Processes controlling the distribution of dissolved Al and Ga along the U.S. GEOTRACES East Pacific Zonal Transect (GP16).

Peng Ho[1]*, Joseph A. Resing[2] and Alan M. Shiller[1]

[1]Division of Marine Science, University of Southern Mississippi, Stennis Space Center, MS 39529, USA

[2]Joint Institute for the Study of the Atmosphere and the Ocean, University of Washington and NOAA-PMEL, 7600 Sand Point Way NE, Seattle, Washington 98115, USA

*Corresponding author: Peng Ho (e-mail: peng.ho@usm.edu; phone: +1-228-688-7093)

Declarations of interest: none

Abstract

Gallium (Ga) behaves similarly to aluminum (Al) in the ocean. However, there are key differences in their behaviors resulting from the small differences in their chemistry. Here we present the distributions of dissolved Ga and Al in the Eastern Tropical Pacific Ocean, obtained as part of the 2013 U.S. GEOTRACES GP16 Eastern Pacific Zonal Transect (EPZT) from Peru to Tahiti. Low surface water dissolved Ga and Al, as well as high and variable surface water Ga/Al ratios along the EPZT reflect low aeolian input and a longer Ga residence time than Al. A gradient of decreasing surface water Ga toward the Peru upwelling region but not seen in surface water Al can be explained by additional dissolved Al inputs from shelf sediments, the presence of less reactive Al species or advection of low-Ga water from elsewhere.

Beyond the coastal upwelling zone, the absence of Ga and Al removal associated with the chlorophyll *a* maximum suggests minimal removal of Al and Ga by biological scavenging in the oligotrophic gyre waters in the EPZT. West of 105°W, an expanding shallow pool (< 200 m) of Ga-enriched water suggests Ga accumulation within the gyre circulation. However, we did not observe dissolved Al enrichment in this Ga-enriched pool. West of 90°W, a dissolved Ga minimum is centered within the nutricline, right below the Ga-enriched pool, and is likely a result of advective input of low-Ga water.

Anomalously high dissolved Al water in the upper 200 m at the middle of the section (106–112°W) was not an artifact of contamination, though the reasons for this remain unknow. Slightly elevated dissolved Al was observed near the Peru margin and at mid-depth in the western part of the section. Surprisingly, this mid-depth dissolved Al enrichment in the west is more prominent than that on the Peru margin. This may result from greater biological Al removal along the margin and/or different dust sources with differing Al solubility. A Ga depletion was commonly observed in the intermediate waters, especially near the Peru margin. This is opposite from the observation of slightly increased Al in these waters and still remains to be explained.

Generally, elevated deep water Ga and Al concentrations were observed in this section, indicating inputs from hydrothermal activity and resuspended sediments. However, ~930 km east of the East Pacific Rise, decreased bottom water Al, even in the nepheloid layer, might be due to low Al dissolution from these resuspended hydrothermal particles and/or the advection of low-Al Pacific Deep Water from the north. West of 143°W, decreased Ga and increased dissolved Al near the bottom indicate Antarctic Bottom Water influence. In the hydrothermal plumes, dissolved Ga and Al behavior is largely regulated by dilution of the hydrothermal signal. Hydrothermal Al flux estimates show hydrothermal inputs of Al are likely to be of regional, not global importance while the hydrothermal Ga flux might be comparable to the aeolian Ga flux.

Keywords: aluminum; gallium; Eastern Tropical Pacific; GEOTRACES; hydrothermal plume; sediment resuspension

1. Introduction

Gallium (Ga) is one position below aluminum (Al) in the Periodic Table, which suggests they are characterized with similar chemical behaviors. Previous studies have indeed shown that Ga in seawater behaves geochemically in manner akin to Al (e.g., Orians and Bruland, 1988a, b; Shiller, 1988). Dissolved Al exhibits a typical scavenged-type distribution in the open ocean (Bruland et al., 2014) and is controlled by various processes including aeolian inputs, particle scavenging, regeneration/remineralization, hydrothermal activities, sediment resuspension and advection (Hydes, 1979, 1983; Measures et al., 1984, 2015; Orians and Bruland, 1985, 1986; Measures and Edmond, 1990; Measures, 1995; Middag et al., 2012, 2013, 2015; Hatta et al., 2013; Grand et al., 2015). Analogous to Al, the oceanic distribution of dissolved Ga is also affected by most, if not all, of these processes; however, Ga is generally less reactive than Al and also less well-studied (Orians and Bruland, 1988 a, b; Shiller, 1998; Shiller and Bairamadgi, 2006).

Although both dissolved Ga and Al are particle reactive and hydrolyzed in seawater, there are key differences in their behaviors resulting from the small differences in their chemistry. In particular, at the pH of seawater, Ga should be dominantly present as $Ga(OH)_4^-$ (Bruland, 1983) while the dominant forms of Al are $Al(OH)_3^0$ and $Al(OH)_4^-$ (Stumm and Morgan, 1996). Because neutral species should be more favored for adsorption onto the net negatively charged surfaces of oceanic particles, it follows that Al should be more readily sorbed by oceanic particle surfaces than Ga (Orians and Bruland, 1988a, b; Shiller, 1988). This results in the shorter residence time of Al in seawater as compared with Ga. For instance, Orians and Bruland (1988a) suggested that in surface waters, dissolved Ga has a residence time of ~decades, which is an order of magnitude longer than the surface water dissolved Al residence time (2–6.5 yrs; Orians and Bruland, 1986; Jickells et al., 1994; Measures and Brown, 1996). In deep waters, Ga has a residence time of ~100–750 years based on simple vertical advection/diffusion modeling (Orians and Bruland, 1988b) while the Al residence time is estimated to be 100–200 years (Orians and Bruland, 1985, 1986), depending on location. Additional chemical factors affecting the two elements are the larger ionic radius of trivalent Ga relative to Al and the longer and more covalent Ga-O bond than Al-O bond (Burton and Culkin, 1972). These two factors suggest that Ga will be more readily leached from solid phases where it substitutes for Al. Both the hydrolysis difference (affecting relative removal of the two elements) and the structural

82 difference (affecting relative input), therefore combine to result in the observed distribution
83 differences of dissolved Ga and Al. Specifically, the high dissolved Ga/Al ratio in surface waters
84 (Orians and Bruland, 1988b; Shiller, 1988, 1998) relative to the crustal ratio (Rudnick and Gao,
85 2014), and the lower inter-basin fractionation of Ga than of Al (Orians and Bruland, 1985,
86 1988b), suggest the interplay of these chemical factors.

87 Major sources for dissolved Al and Ga in surface water include dust deposition and
88 fluvial input. Surface water distributions of Al and Ga suggest that the major source of these
89 elements is aeolian input (Hydes, 1979, 1983; Measures et al., 1984; Orians and Bruland, 1985,
90 1986, 1988a; Shiller, 1998; Shiller and Bairamadgi, 2006). Higher surface water dissolved Al
91 and Ga concentrations in a regime where a high atmospheric dust input occurs (e.g., Hydes,
92 1989; Shiller, 1998; Kramer et al., 2004; Measures et al., 2008a; Middag et al., 2015) reflect the
93 implication of both elements as tracers for dust deposition to the surface ocean. The importance
94 of fluvial inputs for Ga and Al also have been recognized in previous studies (Measures et al.,
95 1984; Kremling, 1985; Shiller and Frilot, 1996; McAlister and Orians, 2012). However, fluvial
96 Al fluxes are commonly removed in river plumes and estuaries (Van Bennekom and Jager, 1978;
97 Morris et al., 1986; Takayanagi and Gobeil, 2000; Brown and Bruland, 2009). In the one study
98 of its estuarine behavior, significant Ga removal was also observed (McAlister and Orians,
99 2012), though how common this is and the relative estuarine removal of Ga versus Al is not
100 known. Anthropogenic Ga input to the surface ocean both through dust (Shiller, 1998; Shiller
101 and Bairamadgi, 2006) and fluvial input (Shiller, 1988; Shiller and Frilot, 1996) appears to be
102 minor. Possible sources for Al and Ga throughout the water column include reversible exchange,
103 regeneration, and remineralization (Orians and Bruland, 1985, 1986, 1988a, b). Since Ga and Al
104 have hydrolysis chemistry similar to that of thorium (Th), reversible exchange on particles in the
105 water column was suggested as a source of deep Ga and Al; however, no direct evidence has
106 been found for this mechanism (Orians and Bruland, 1988a, b; Bruland et al., 2014). Middag et
107 al. (2015) proposed that the well-correlated Si-Al relationship in some basins is due to
108 regeneration/remineralization from settling biogenic particles. They also observed a positive
109 correlation between Al and apparent oxygen utilization (AOU) in the oxygen minimum zone
110 (OMZ) in the western equatorial Atlantic Ocean (between the equator and 10°N), indicating Al
111 release from remineralization. However, Measures et al. (2015) did not observe this positive
112 relationship in the OMZ off the northwest African coast, instead finding that Al minimum

corresponded with the oxygen minimum. Like Al, regenerated Ga from settling particulate matter and remineralization at the sediment-water interface were suggested as sources for Ga to the water column (Orians and Bruland, 1988a, b). The bottom sources for Ga and Al can be sediment fluxes (i.e., pore water, remobilization at the sediment surface) and sediment resuspension (Orians and Bruland, 1986, 1988a, b; Measures, 1995; Shiller, 1998; Hatta et al., 2013; Middag et al., 2012, 2013, 2015; Grand et al., 2015). Increased dissolved Al and Ga in the deep water have been attributed to resuspended sediments and subsequent dissolution of Al and Ga (e.g., Orians and Bruland, 1986; Moran and Moore, 1991; Shiller, 1998; Measures et al., 2015) and/or the release of diagenetically Al-enriched porewaters (e.g., Middag et al., 2012, 2013; Hatta et al., 2013). Along with Al and Ga enrichments in hydrothermal vent fluids (Von Damm et al., 1985; Metz and Trefry, 2000), elevated dissolved Al and Ga in the deep water near the mid-ocean ridges (Stoffyn and Mackenzie, 1982; Lupton et al., 1993; Shiller et al., 2014; Measures et al., 2015; Resing et al., 2015) suggests hydrothermal inputs for Al and Ga in the deep water. However, Middag et al. (2015) argued that hydrothermal source for Al is minor on the basin-wide scale, which is supported by reports of insignificant hydrothermal Al fluxes (Lunel et al., 1990; Elderfield and Schultz, 1996).

Evidence of Al and Ga removal by particle scavenging has been seen throughout the water column (Hydes, 1979; Orians and Bruland, 1985, 1986, 1988a, b; Shiller, 1998; Middag et al., 2015). For Al, the removal mechanism probably involves both passive and active scavenging by biogenic particles, likely associated with silica (Hydes, 1979; Moran and Moore, 1988, 1992; Gehlen et al., 2002; Koning et al., 2007; Li et al., 2013). In contrast, the understanding of Ga scavenging removal has not received much attention. Given that Ga competes with Fe for binding to siderophores (Emery and Hoffer, 1980; Emery, 1986; Gascoyne et al., 1991), Ga could be removed via active scavenging. Low surface water dissolved Ga and Al concentrations in high productivity waters, relative to their concentrations in open gyre waters, are likely caused by intensive scavenging by biogenic particles (Orians and Bruland, 1986, 1988a; Shiller, 1998; Brown and Bruland, 2009).

The advection of low or high dissolved Ga and Al from areas of low or high dust input also affects the distributions of these elements. For example, minima of Ga and Al at mid-depth observed in the Atlantic and North Pacific are indicative of the advection of low-Ga and low-Al

waters from higher latitudes where there is lower dust deposition (Measures and Edmond, 1990; Measures, 1995; Shiller, 1998; Shiller and Bairamadgi, 2006; Middag et al., 2015). Likewise, dissolved Al characteristic of Subtropical Mode Water has been observed advected away from source regions (Measures et al., 1986, 2008a, 2015; Middag et al., 2015). Maxima of Ga and Al have been observed in waters influenced by the Mediterranean Outflow Water (Measures, 1995; Shiller, 1998; Shiller et al., 2014; Measures et al., 2015). Additionally, Shiller and Bairamadgi (2006) suggested that a Ga maximum in subsurface waters in the northeast Pacific Ocean (Orians and Bruland, 1988a, b) was likely caused by transport of high Ga waters rather than from in situ Ga regeneration.

Given the differing reactivities of these two similar elements, examination of dissolved Ga/Al ratios in the water column can reveal the effect of biogeochemical and physical processes on their distributions. Shiller and Bairamadgi (2006) found that the dissolved Ga/Al ratio varied with chlorophyll *a* (Chl *a*) in northwest Pacific surface waters, probably because of a faster scavenging removal of Al than Ga. An implication of this relationship is that the Ga/Al ratio might be used to minimize the uncertainty of surface Al residence time used in Al-based dust deposition models (Shiller and Bairamadgi, 2006). In deep waters, the change of dissolved Ga/Al ratio between different water masses (e.g., Ga/Al ratio in North Atlantic Deep Water: ~2 mmol/mol; Ga/Al ration in Antarctic Bottom Water: ~4 mmol/mol) suggests the possibility of different enrichment mechanisms causing differing ratios in these water masses (Shiller and Bairamadgi, 2006).

Despite the knowledge of oceanic dissolved Ga and Al distributions outlined above, distributions of these two elements in the southeastern tropical Pacific Ocean are largely unknown. We present here dissolved Al and Ga data collected from the U.S. GEOTRACES GP16 East Pacific Zonal Transect (EPZT). A variety of biogeochemical and physical processes (i.e., Peru upwelling, extreme OMZ, and hydrothermal plumes) in our study area provide an opportunity to further examine the processes and mechanisms that control oceanic Al and Ga distributions. Although the dust deposition in the South Pacific Ocean is not as significant as in the North Atlantic Ocean, biogenic removal and shelf sediment input might be important sinks/sources for Al and Ga in the Peru upwelling region. This transect also showed a strong westward transport of hydrothermal plume waters from the East Pacific Rise (EPR) and a hydrothermal dissolved Al signal was observed as far as ~3000 km west of the EPR (Resing et

al., 2015; Jenkins et al., 2018). Thus, hydrothermal activity might be a potential source for Ga as well. Benthic nepheloid layers were commonly observed near the bottom across the transect (Lee et al., 2018; Ohnemus et al., 2018) providing an opportunity to evaluate the role of resuspended sediments for deep Al and Ga.

2. Methods

2.1 Seawater Sampling

Water samples were collected at 35 stations from the R/V Thomas G. Thompson during the U.S. GEOTRACES GP16 EPZT expedition (Fig. 1), conducted October 25–December 20, 2013 from Manta, Ecuador to Papeete, French Polynesia. Various station types were occupied in the EPZT: four shelf stations (1–2 casts), 13 full depth stations (3 casts), 13 shallow stations (1 cast, depth ~1000 m) and 5 super-stations (3–4 casts).

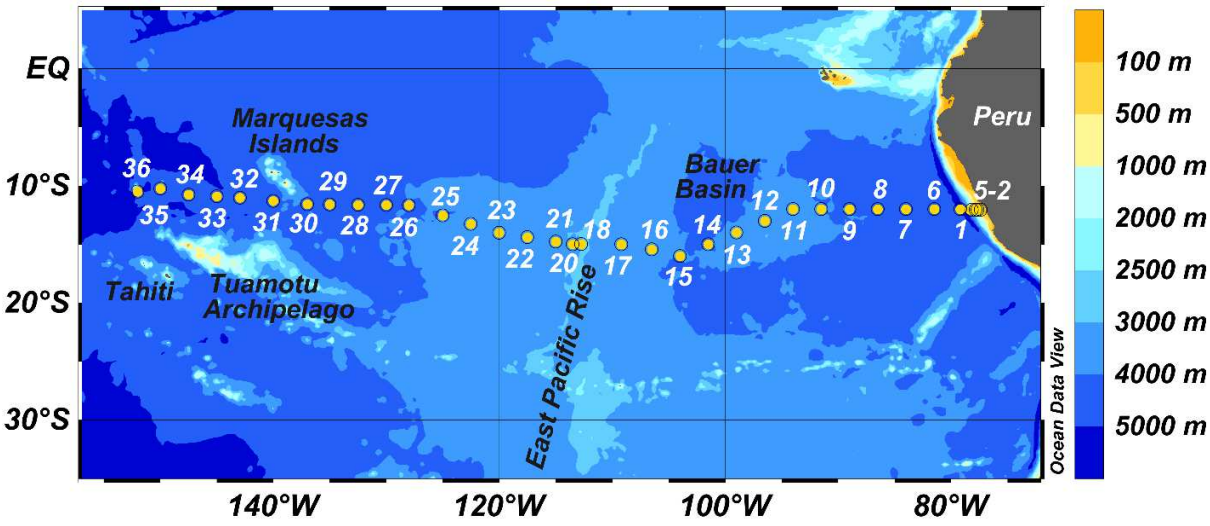

Figure 1. Cruise track of the U.S. GEOTRACES GP16 East Pacific Zonal Transect (EPZT). Note that station 1 (Peru-Chile Trench) is out of numerical order and is located between stations 5 & 6.

Water column samples were obtained using 12-L Teflon-coated GoFlo bottles deployed on the trace metal clean GEOTRACES carousel (Cutter and Bruland, 2012). Water samples were filtered through 0.2 µm capsule filters (Pall Acropak Supor capsule) and collected using trace-metal-clean protocols (Measures et al., 2008b; Cutter et al., 2014). Surface water samples (4 m

depth) were obtained using an underway towed-fish system (Bruland et al., 2005) and filtered through a 0.45 µm Osmonics and a 0.2 µm polycarbonate cartridge filter.

For Ga samples, the filtered samples (~125 mL) collected from the GoFlo bottles were stored in pre-cleaned HDPE bottles and shipped back to the laboratory for acidification and analysis. After samples were transported to the laboratory, an aliquot of ultrapure 6 N HCl (Seastar Baseline) was added to the sample to reduce the pH to ~1.8 and the sample was then stored at room temperature. For Al samples, filtered samples were stored in 100-mL LDPE bottles and were acidified with 12 N ultrapure HCl (Fisher Optima) to pH ~1.7 at sea. Ancillary data (e.g., salinity, temperature, nutrients, oxygen) was provided by the cruise management team and can be found at the BCO-DMO data repository (http://www.bco-dmo.org/project/499723).

2.2 Analytical Method

2.2.1 Ga

Ga was concentrated using an isotope dilution, magnesium hydroxide co-precipitation method (Shiller and Bairamadgi, 2006 as modified from Wu and Boyle (1997, 1998)) and analyzed using ThermoFisher Element XR sector field inductively coupled plasma-mass spectrometer (ICP-MS) with a PFA microflow nebulizer (Elemental Scientific, Inc.).

Briefly, acidified seawater samples (7 mL) were spiked with a known amount of enriched isotope of 99.8% ^{71}Ga (Oak Ridge National Laboratory), following by adding ~60 µL of clean ammonia to form a small amount of magnesium hydroxide precipitate. Centrifugation allowed removal of the interfering, salty supernatant. Trial results showed an interference of doubly charged ^{138}Ba on ^{69}Ga. In order to minimize the Ba^{2+} inference, precipitates were rinsed three times with purified 0.1% NH_4OH (Seastar Baseline), centrifuging the sample and removing the supernatant between each rinse. The final, washed precipitate was then dissolved in 275 µL ultrapure 3% HNO_3 and analyzed in low resolution on the ICP-MS, monitoring ^{69}Ga, ^{71}Ga, and ^{138}Ba. The interference of Ba^{2+} was generally less than 0.2%. A minor correction for residual Ba was made based on the ratio of $^{138}Ba^{++}/^{138}Ba^{+}$ counts in a Ba standard solution. For data points that did not fit in the vertical profile shape, we prepared another fresh sample to reanalyze. When the re-analyzed value fit the vertical profile, we reported the results from the reanalysis.

Otherwise, we averaged all results when the re-analyzed value agreed with the original values (the difference is mostly less than 2 s.d. = 3.0 pmol/kg).

US GEOTRACES intercalibration samples and in-house reference solutions were run during each analysis. Dissolved Ga concentrations were 42.5 ± 1.7 pmol/kg (n = 20) for GS and 32.7 ± 1.4 pmol/kg (n = 18) for GD, respectively. For in-house reference solutions, averaged Ga was 16.9 ± 0.9 pmol/kg (n = 37). The limit of detection for Ga was 1.5 pmol/kg. Recovery of the method, as determined by repeated analysis of a spiked and unspiked seawater sample was 101.3 ± 4.7%.

2.2.2 Al

Dissolved Al was measured on board ship using a modified Flow Injection Analysis (FIA) method with in-line preconcentration and fluorometric detection (Resing and Measures, 1994). In the modified FIA method, Toyopearl AF-Chelate 650M was used to preconcentrate Al and acidified deionized water was the carrier (Resing et al., 2015). Repeated runs of internal and primary standards suggest a precision of ± 4.2%. Additionally, two internal reference standards and SAFe reference samples were analyzed as well. Two internal reference standards were run during the cruise, with dissolved Al concentrations of 1.65 ± 0.24 nM (± 15%; n = 118) and 1.98 ± 0.07 nM (± 3.4%; n = 75), respectively. The two internal standards during the cruise reflect an increase in precision and accuracy in the latter half of the cruise. Our overall precision and accuracy ranged from ± 0.2 nM early in the cruise (east) to ± 0.1 nM later in the cruise at the westernmost stations. We estimate our limit of detection to be ≈ 0.3 nM; however, a linear regression for the values obtained here for the GEOTRACES reference materials versus the consensus values yields an intercept of 0.5 nM (also discussed in Resing et al., 2015), suggesting that the values reported here may reflect an offset of this magnitude. However those standards are stored in bottles with polypropylene caps which are known to contaminate for Al, and thus it is unclear if the reference materials retain their original concentrations; we thus report the values that we determined without accounting for any offset. In terms of the quantitative interpretation of our data, this would only be important for the very low dissolved Al concentrations in our shallowest samples.

Both dissolved Al and Ga data are available through the BCO-DMO data repository (http://www.bco-dmo.org; datasets 503133 and 756982).

252 *2.3 Conservative Ga estimates*

253 Water mass analysis combined with published Ga data allows for the estimation of a
254 'conservative' Ga distribution in this section. Through comparisons between our observed Ga
255 concentrations and the conservative Ga estimates, we can evaluate the extent to which observed
256 changes in Ga concentrations resulted from simple mixing versus biogeochemical processes in
257 this transect. An Optimum Multiparameter Analysis (OMPA) of tracer distributions in the GP16
258 section was previously conducted by Peters et al. (2018). Along the EPZT, Peters et al. (2018)
259 divided the water column into three discrete zones: thermocline (26.0 kg $m^{-3} \leq \sigma_0 \leq$ 27.0 kg m^{-3}),
260 intermediate (27.0 kg $m^{-3} < \sigma_0 \leq$ 27.72 kg m^{-3}) and deep water ($\sigma_0 >$ 27.72 kg m^{-3}). Thermocline
261 water masses include the Equatorial Subsurface Water (ESSW), Eastern South Pacific
262 Intermediate Water (ESPIW) and South Pacific Central Water (SPCW). Intermediate water
263 masses include Antarctic Intermediate Water (AAIW), Equatorial Pacific Intermediate Water
264 (EqPIW), Upper Circumpolar Deep Water (UCDW) and Pacific Deep Water (PDW). Deep water
265 masses include UCDW, PDW, Lower Circumpolar Deep Water (LCDW) and Antarctic Bottom
266 Water (AABW). More details of this OMPA analysis are described in Peters et al. (2018).
267 Because data on the distribution of dissolved Ga are limited, we were not able to determine the
268 dissolved Ga concentration of all of the exact water types chosen by Peters et al. (2018). Thus,
269 we present a range of scenarios representing both mean and extreme choices of end-member
270 concentrations in an effort to show that these different choices, while affecting the magnitude of
271 the apparent non-conservative Ga behavior, do not alter the overall pattern of source versus sink.

272 For AAIW, AABW, UCDW and PDW, Ga endmember estimates in these water masses
273 were reported previously (Shiller, 1998; Shiller and Bairamadgi, 2006). Although their sampling
274 stations were located in the South Atlantic and North Pacific Oceans, not close to the GP16
275 stations, we selected the closest locations to the geographic regions of water masses defined by
276 Peters et al. (2018). Additionally, we compared previously reported characteristics (i.e., potential
277 temperature, salinity, dissolved oxygen, or nutrients) in these water masses (where available)
278 with those of the water masses selected by Peters et al. (2018) to help verify our selection (see
279 details in the Supplementary Materials).

280 There were no reference values for Ga endmembers in the ESSW, ESPIW, SPCW,
281 EqPIW and LCDW. However, our Ga data allows for Ga endmember estimates in EqPIW,

ESSW and SPCW since the Peters et al. (2018) analysis results in some GP16 samples having a 100% contribution of these water types. Thus, we plotted Ga concentration versus water mass fraction (EqPIW, ESSW, SPCW) to find Ga endmembers in these water masses (Figs. S1 and S2). Although the contribution of ESPIW in samples ranged from 0% to 76%, only a small variation (± 2 pmol/kg) of Ga concentration was observed in ESPIW-dominant (> 40 %) samples (Fig. S1). Thus, the ESPIW Ga endmember estimate was obtained by extrapolation of the Ga vs %ESPIW relationship. The lack of dominant LCDW in samples (LCDW contribution < 54%) and no reported LCDW Ga in previous studies make LCDW Ga estimates difficult. However, based on its origin and flow path (Talley et al., 2011), we assumed that Ga in LCDW is somewhere between that of AABW and North Atlantic Deep Water. Our selection of Ga endmember concentrations for each water type are listed in Table 1; further detail on the endmember Ga concentration selection can be found in the Supplementary Material.

The 'conservative' Ga estimate is a sum of the contribution of Ga from each water mass:

$$conserva\ \ ve\ \ \ a = \sum_{i=1}^{n}\ \ a_i \times frac\ \ on_i$$

Here Ga_i is the Ga endmember in water type i and $fraction_i$ is the percent contribution of water type i to the samples. The difference of conservative Ga from observed Ga can thus be an indicator of the extent of non-conservative Ga behavior. Ga is removed from the water column when conservative Ga is higher than observed Ga. Lower conservative Ga than observed Ga suggests additional sources for Ga in the water column.

Because we could only provide estimated ranges for some of the Ga endmember concentrations, different scenarios (i.e., different values used for endmembers; shown in Table S1) are presented here (Fig. S4), which illustrate the uncertainty, to some extent, of conservative Ga.

Water Mass	Ga endmember (pmol/kg)	Reference Location	Reference
Thermocline Layer			
ESSW	7-10	EPZT	this study
ESPIW	6-8	EPZT	this study
SPCW	7-9	EPZT	this study
Intermediate Layer			
AAIW	7-15	south and central Atlantic Ocean	Shiller (1998); Shiller and Bairamadgi (2006)
EqPIW	7-9	EPZT	this study
Intermediate/Deep Layers			
UCDW	20-25	south Atlantic Ocean (33°S, 40°W)	Shiller (1998)
PDW	22-28	near Hawaii (22°45'N, 158°W)	Shiller and Bairamadgi (2006)
Deep Layer			
LCDW	30-35		
AABW	25-30	south and central Atlantic Ocean	Shiller and Bairamadgi (2006)

Table 1. Ga endmember estimates in water masses of GP16 OMPA. These Ga endmembers were used for estimating conservative Ga concentrations in GP16 samples. There are no available published Ga data for LCDW and no means for directly estimating Ga in LCDW from our data. Ga in LCDW was roughly estimated by assuming a concentration range between that of AABW and NADW.

3. Results and Discussion

3.1 Overview of dissolved Ga and Al distributions across the transect

Dissolved Ga concentration was generally low (< 12 pmol/kg) in the upper water column (0–1000 m) and increased with depth between 1000 and 3500 m (Fig. 2a, b). Below this, Ga was nearly constant (29.5 ± 2.7 pmol/kg) in the deep water (starting at 2500–3500 m), with the exception of hydrothermal plume waters near the EPR (Stns. 18–21) and deep waters at the western-most stations (Stns. 32–36) (Fig. 2a, b).

In shallow waters (150–300 m) of the North Pacific, Orians and Bruland (1988a) found a dissolved Ga maximum in subsurface water which they attributed to reversible exchange of Ga with particle surfaces (Bacon and Anderson, 1982). However, little evidence of this subsurface Ga maximum was seen in the Atlantic Ocean or the northwest Pacific Ocean (Shiller, 1998; Shiller and Bairamadgi, 2006) nor is it observed in our eastern tropical Pacific Ocean section. Thus, the subsurface Ga maximum in the North Pacific Ocean is likely caused by advection, as Shiller and Bairamadgi (2006) suggested.

The absence of a dissolved Ga minimum at mid-depth in the EPZT section (Fig. 2a, b) differs with previously published Ga profiles in other ocean basins (Orians and Bruland, 1988a, b; Shiller, 1998; Shiller and Bairamadgi, 2006). Specifically, an intermediate water Ga minimum was observed in the Atlantic (700–1000 m) and the North Pacific Oceans (~500–1000 m) (Orians and Bruland, 1988a, b; Shiller and Bairamadgi, 2006). While Orians and Bruland (1988b) argued that the intermediate water Ga minimum was caused by Ga scavenging, Shiller and Bairamadgi (2006) suggested it resulted from advection of low Ga intermediate waters formed in low dust surface outcrops.

The steady depth increase of dissolved Ga in the mid-water column and relatively constant concentrations in the deep water across most of the transect (Fig. 2a, b) is similar to some of the Ga profiles previously reported in the Atlantic and Pacific Oceans (Shiller and Bairamadgi, 2006). A slight increase in dissolved Ga was seen in the hydrothermal plume near the EPR (Fig. 2a). Likewise, additional Ga from the Mid Atlantic Ridge (MAR) was observed in the North Atlantic Ocean during the GEOTRACES GA03 North Atlantic Zonal Transect cruise in 2011 (Shiller et al., 2014). In spite of limited Ga data in hydrothermal plume waters, our

results combined with enriched Ga in hydrothermal vent fluids (German and Seyfried, 2014) suggest a small but noticeable hydrothermal source for Ga in the deep water.

As we described earlier (Section 2.3), the difference between observed and conservative Ga distributions can help us evaluate dissolved Ga behavior in the EPZT. Most scenarios showed that the difference between observed and conservative Ga was very small in the thermocline layer while conservative Ga differed significantly from observed in the intermediate and deep waters (Fig. S4; an average of all the scenarios is shown in Fig. 2c). In the intermediate layer, observed Ga was lower than conservative, indicating Ga is removed from the water (Figs. 2c and S4). However, in deep waters, the observed Ga was higher than conservative at most stations, except at the western-most stations (Stns. 32 and 36; Figs. 2c and S4) where the observed Ga was slightly lower than conservative. Only Scenario 2 (Fig. S4), which used high Ga values for the endmember concentrations of each water type (Table S1), showed Ga removal in the thermocline and intermediate layers and conservative behavior in most of the deep waters, with a slight addition of Ga in the hydrothermal plume near the EPR. Despite the slight deviations among the different endmember scenarios, all of the scenarios suggest that Ga behaves non-conservatively throughout most of water column in the EPZT (Figs. 2c and S4), in general agreement with the prevailing view of the oceanic Ga distribution.

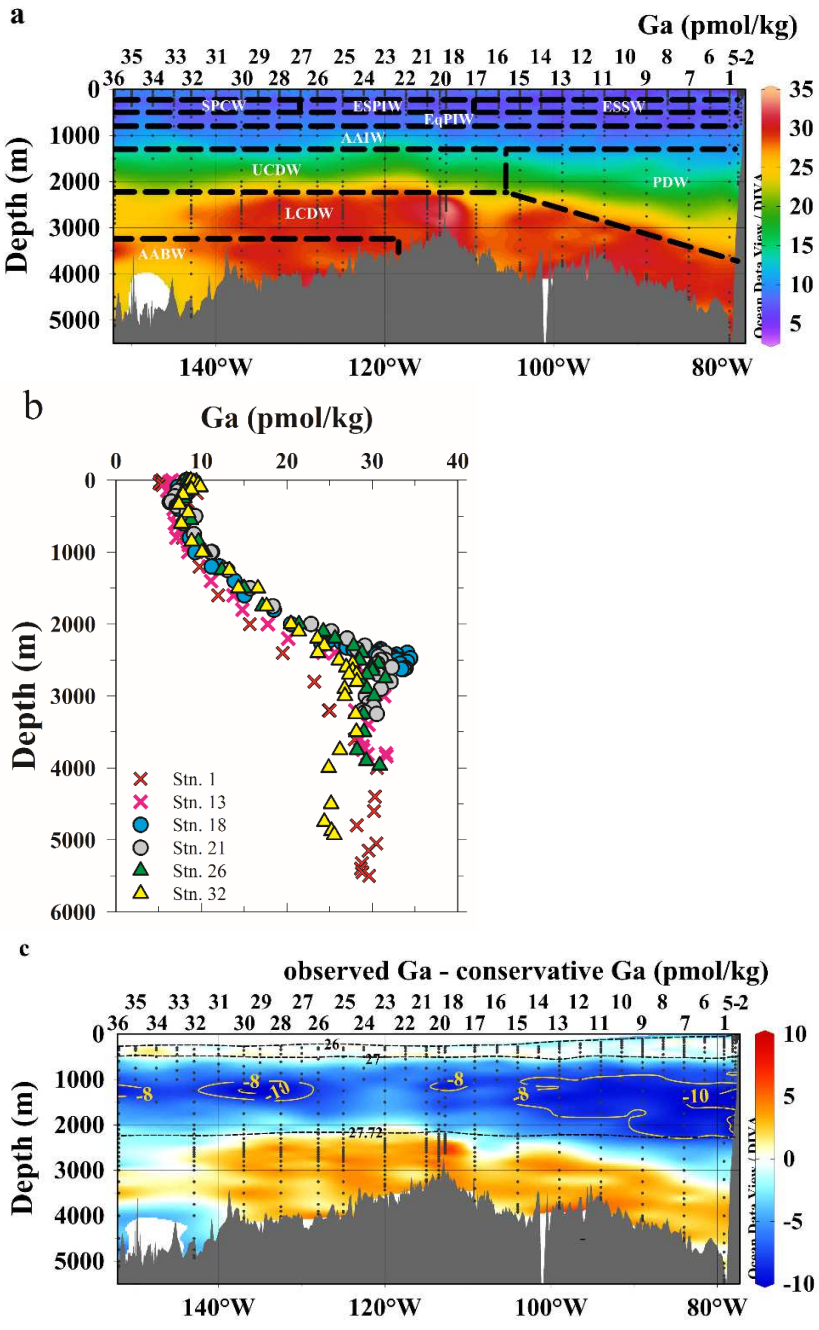

Figure 2. (a) The distribution of dissolved Ga concentration along the EPZT. Dashed lines indicate predominant water types across the section from the OMPA results of Peters et al. (2018).(b) Ga profiles at various stations (Stns. 1, 13, 18, 21, 32 and 36). Note that Stn. 18 was located near the crest of the East Pacific Rise. (c) The difference between observed Ga and conservative Ga shown is an average of all the scenarios here (see text). Dashed lines show isopycnal surfaces (σ_0 = 26.0 kg m^{-3}, σ_0 = 27.0 kg m^{-3} and σ_0 = 27.72 kg m^{-3}). Yellow contours indicate where the greatest Ga depletion was observed. The results of individual scenarios can be found in Fig. S4.

Dissolved Al (dAl) results for the EPZT were presented by Resing et al. (2015), with a focus on the hydrothermal plume. In this manuscript, we describe the dAl distribution across the entire transect and investigate possible mechanisms controlling its distribution. Dissolved Al was commonly low (< 3 nmol/kg) in the upper and middle layers in the EPZT (Fig. 3). Three areas of increased dAl were observed in the section (Fig. 3): (1) abnormally high dAl (4–32 nmol/kg) in subsurface waters (20–150 m) at Stns. 16–18, (2) hydrothermal plume waters from Stn. 18 to Stn. 26 and (3) deep waters near the bottom (east of the EPR: ~800–1500 m above bottom; west of the EPR: ~1000–2400 m above bottom). Dissolved Al profiles in the Atlantic and Pacific Ocean have been classified as showing a scavenged-type distribution, with high surface dAl, a mid-depth dAl minimum and increased bottom dAl (Hydes, 1979; Orians and Bruland, 1985, 1986; Measures et al., 1986, 2005; Measures, 1995). In contrast, the dAl minimum was absent in the intermediate water in the EPZT (Fig. 3). Instead, dAl concentrations were generally homogeneous (~1–2 nmol/kg) between 500 and 2000 m, except for slowly increasing dAl with depth at Stn. 36 (Fig. 3). Elevated dAl was observed in the hydrothermal plume and extended westward > 3000 km (Fig. 3; Resing et al., 2015). In general, a small increase in dAl near the bottom (Fig. 3) was coincident with bottom nepheloid layers across the transect (Ohnemus et al., 2018), except in the bottom waters at Stns. 15–17 (immediately east of the EPR). At almost all stations, the bottom layer also showed increased dissolved ^{232}Th (d^{232}Th) (Pavia et al., 2018) as well as particulate Ti (pTi) and Al (pAl) (Lee et al., 2018), all lithogenic elements suggestive of sedimentary sources. Moreover, resuspended sediments in bottom nepheloid layers also resulted in the intensive scavenging of d^{230}Th and dissolved ^{231}Pa (Pavia et al., 2018), especially east of the EPR. This suggests that resuspended sediment is a source of deep Al in the EPZT, in agreement with previous observations (Orians and Bruland, 1986; Moran and Moore, 1991; Measures et al., 2015).

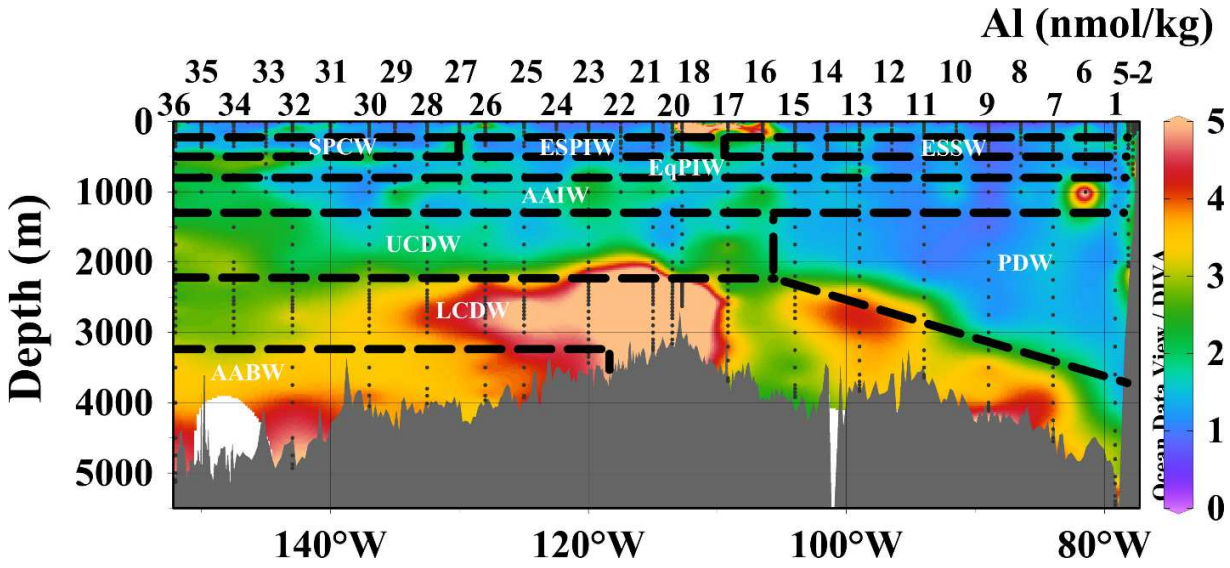

Figure 3. The distribution of dissolved Al concentration along the EPZT. Dashed lines indicate predominant water types across the section from the OMPA results of Peters et al. (2018).

Similar to previously reported Ga profiles, a dAl minimum has been observed in intermediate waters in various ocean basins, and could be caused by either scavenging (e.g., Hydes, 1979; Orians and Bruland, 1986, 1988a; Bruland et al., 1994) or advection of low-Al water masses (Measures, 1995). However, a dAl minimum was not distinct in intermediate waters of the EPZT. In EPZT intermediate waters, dAl ranges from 0.8–5.5 nmol/kg, similar to intermediate water dAl in the North Pacific (0.5–2 nmol/kg; Orians and Bruland, 1985, 1986, 1988a; Measures et al., 2005) and South Atlantic (2–6 nmol/kg; Measures and Edmond, 1990; Middag et al., 2015) Oceans, but an order of magnitude lower than in North Atlantic intermediate waters (10–20 nmol/kg; Measures et al., 2015; Middag et al., 2015). This suggests the homogeneous dAl concentration in the upper water column (500–2000 m) along the EPZT might be a result of low dust deposition in the South Pacific Ocean (Mahowald et al., 2005; Grand et al., 2014; Zhang et al., 2015). In the upper intermediate layer (500–1000 m) of the EPZT section, waters consisted of a mixture of AAIW (~40%) and EqPIW (~60%) (Peters et al., 2018). Previously, it has been shown that AAIW is characterized with low Al due to low dust deposition in high-latitude regions (Van Beusekom et al., 1997; Middag et al., 2011, 2015). Transport of low-Al AAIW in the South Atlantic has been observed at mid-depth (Measures,

1995). For the origin of EqPIW, Peters et al. (2018) selected a location near the equator (at 829m, 5°S, 110°W) where dust deposition also appears to be low (Mahowald et al., 2005). We thus suspect that Al in EqPIW is fairly low as well. Low Al was expected in both water masses (AAIW and EqPIW) due to their origins in low dust deposition regions. However, low Al was not distinct in the intermediate water across the transect (Fig. 3). We suspect that a combination of low scavenging rate and low dust deposition in this region might be responsible for the absence of Al minimum in the intermediate waters.

Given that the spatial (horizontal and vertical) variations of dissolved Ga/Al ratios reflect differential input and/or removal of Ga and Al, their ratio also can be a proxy to identify what processes control their behaviors. In the EPZT, a distinct feature is a mid-depth belt of elevated Ga/Al ratio across the transect (Fig. 4), in the depth range of the mid-water Ga gradient and relatively low dAl (Figs. 2 and 3; see also Section 3.3). Decreased Ga/Al ratios near bottom across the transect likely reflect increased bottom dAl due to sediment resuspension, as well as relatively high dAl accumulated along the flow path of AABW (Figs. 3 and 4).

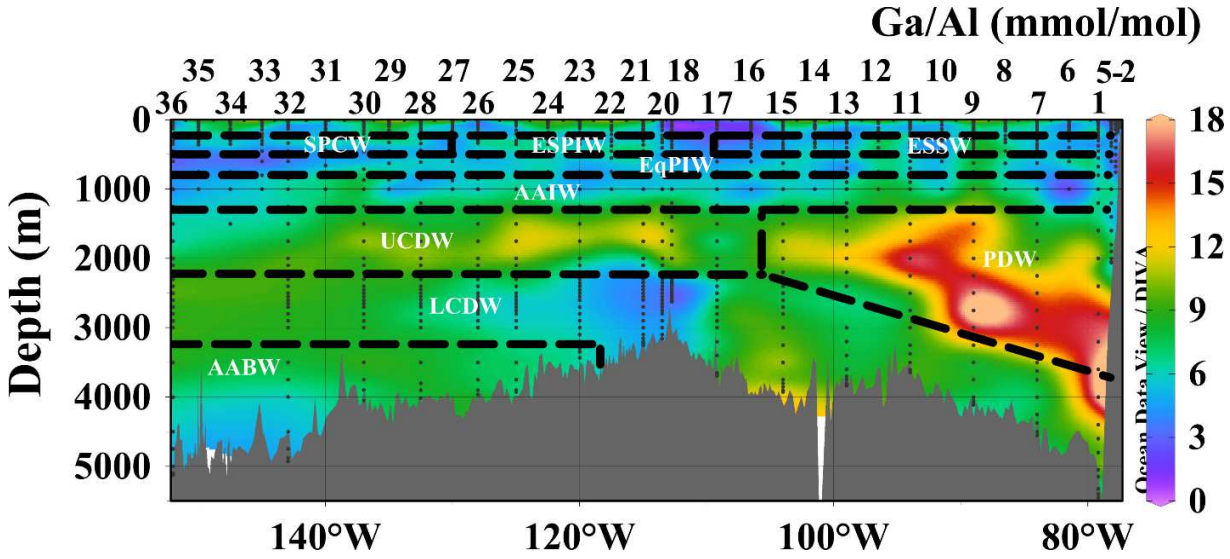

Figure 4. The distribution of dissolved Ga/Al ratios in the EPZT. Dashed lines indicate predominant water types across the section derived from OMPA results of Peters et al. (2018).

3.2 Dissolved Ga and Al in the upper water column

3.2.1 Surface waters

Surface water dissolved Ga ranged from 4 to 11 pmol/kg, with decreasing Ga from the central gyre toward the Peru coast (Fig. 5). A similar horizontal gradient in the surface Ga distribution was observed in the northeast subtropical Pacific as well, with a range of 2–12 pmol/kg (Orians and Bruland, 1988a). Relatively low Ga (generally 4–6 pmol/kg) in the upper 50 m at the coastal stations (Stns. 1–6) coincided with elevated total Chl *a* concentration (Fig. 6a, c), implying the removal of Ga via biological scavenging. Alternatively, these low-Ga waters near the Peru coast might be advected from elsewhere although our discussion is limited by the lack of dissolved Ga measurements in the South Pacific. Along the Peru margin, there is an equatorward surface current related to the Peru Coastal Current and Peru Oceanic Current (Wyrtki, 1966; Strub et al., 1998) that deliver cold water from the south (Chaigneau et al., 2013). Although dust deposition models (e.g., Jickells et al., 2005) show some localized increase in dust deposition to the coastal waters along the northern Chilean margin, predicted Al for those waters is still low and thus we assume that the dissolved Ga is also low. Upwelling is another factor that could influence the Ga distribution in our margin stations; however, increasing Ga with depth in the upper 200 m at Stns. 1–6 (Fig. 6a) suggests that low Ga at the surface was not derived from upwelled water. Despite not being able to pinpoint a source of low Ga water for the Peru margin, we do note that there was a linear correlation between salinity and surface Ga at Stns. 1–15 (R^2 = 0.6, $p < 0.0001$; Fig. 7), suggesting a contribution of physical mixing for the observed surface water Ga gradient on the first half of the transect.

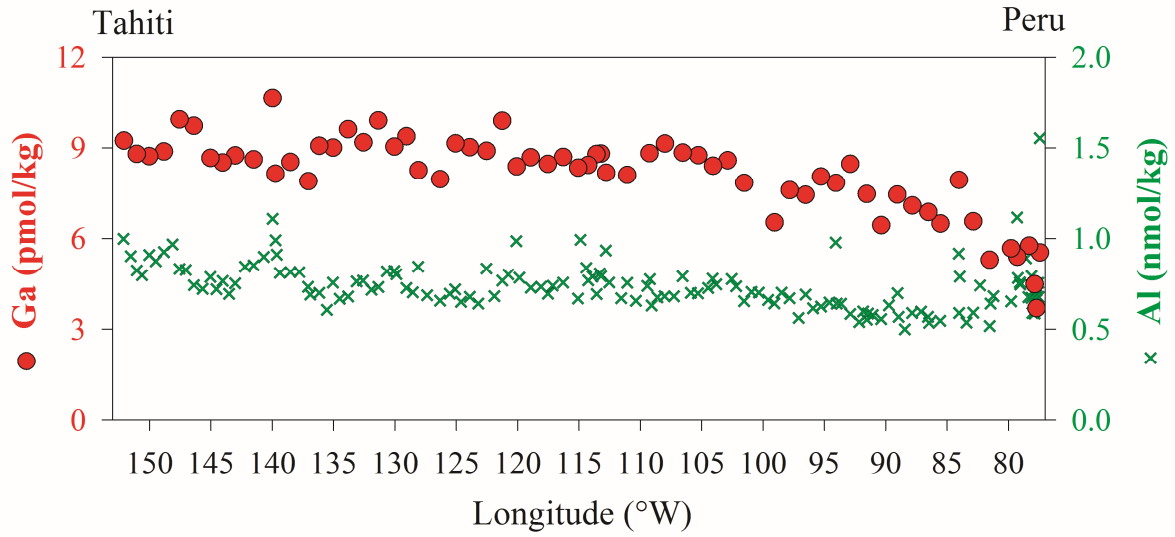

Figure 5. The distributions of dissolved Ga (red circles) and Al (green crosses) in surface waters along the EPZT.

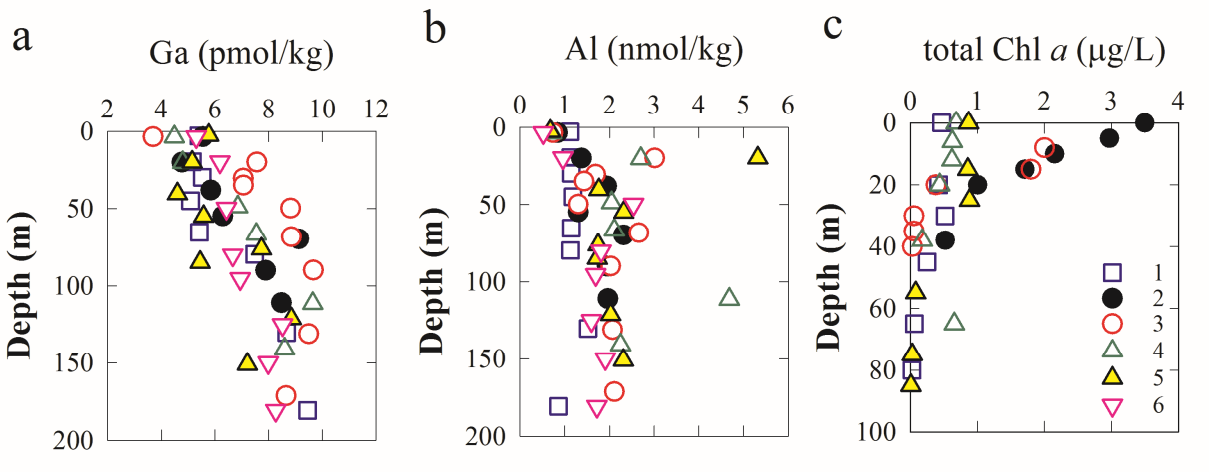

Figure 6. Vertical distributions of dissolved (a) Ga and (b) Al in the upper 200 m near the Peru coasts (Stns. 1–6). (c) Total Chl *a* concentration distribution in upper 100 m at Stns. 1–5, pigment samples were not collected at Stn. 6.

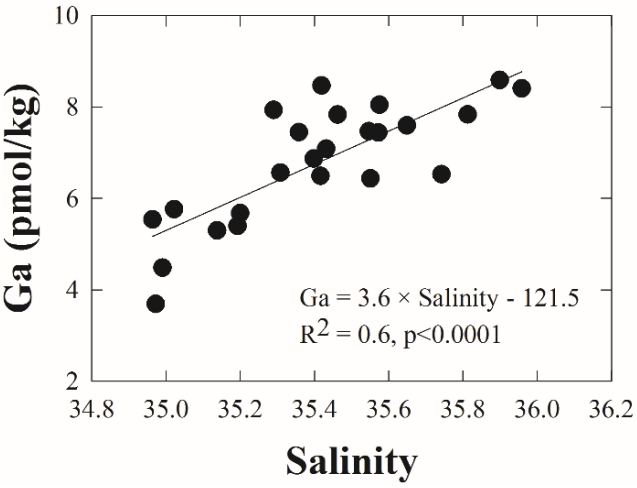

Figure 7. Surface water dissolved Ga concentration in the first half of the EPZT section (Stns. 1–15) as a function of salinity.

462 Surface water Al (< 4 m) concentrations ranged from 0.5 to 1.6 nmol/kg (Fig. 5) which is
463 close to the average dAl (0.6–2.2 nmol/kg) in the mixed layer at most stations, and these
464 concentrations are similar to the range predicted from dust deposition by Han et al. (2008).
465 However, mixed layer dAl at Stns. 16 and 18, with average dAl concentrations of 17 nmol/kg at
466 Stn. 16 and of 15 nmol/kg at Stn. 18, deviated significantly from the very surface dAl
467 concentrations (0.8 and 0.9 nmol/kg, respectively).

468 Surface dAl values were relatively low in the Eastern Tropical Pacific Ocean, compared
469 with surface dAl in the North Atlantic Ocean (average mixed layer dAl: ~9–43 nmol/kg) where
470 high dust input contributes to elevated surface water Al (Measures et al., 2015). Likewise,
471 surface Ga in the Eastern Tropical Pacific Ocean (this study) was lower than published surface
472 Ga (28-59 pmol/kg) in the Atlantic Ocean (Shiller, 1998; Shiller and Bairamadgi, 2006). It does
473 make sense that we observed relatively low Ga and Al in surface waters along the EPZT due to
474 low dust input in this study area (Mahowald et al., 2005). This observation is also supported by
475 observation of low pAl concentrations in the EPZT (Lee et al., 2018) relative to pAl in the North
476 Atlantic Ocean (Ohnemus and Lam, 2015). Again, the concentrations of dissolved Ga and Al in
477 surface waters reflect the amount of dust deposition, consistent with the observations in previous
478 studies (Orians and Bruland, 1988a, b; Hydes, 1989; Measures and Edmond, 1990; Shiller, 1998;
479 Kramer et al., 2004; Shiller and Bairamadgi, 2006; Measures et al., 2008a; Middag et al., 2011,
480 2015). In comparing the surface water dissolved Ga and Al concentrations between the EPZT
481 section and the North Atlantic (GEOTRACES GA03), we note the greater relative inter-ocean
482 difference for Al versus Ga, which is consistent with a shorter residence time of Al than Ga.

483 Low surface Al (0.3–0.8 nmol/kg) was seen in the high productivity waters off the
484 California coast, with a gradient of increasing Al concentration toward the North Pacific
485 subtropical gyre region (Orians and Bruland, 1986; Measures and Edmond, 1990; Johnson et al.,
486 2003; Measures et al., 2005; Brown and Bruland, 2009). In contrast, a surface Al gradient was
487 not apparent across our transect (Fig. 5). The lack of dissolved Al depletion in the upper 200 m
488 near the Peru coast (Stns. 1–6) (Fig. 6b, c) raises an obvious question of why we do not observe
489 diminished dAl near the Peru margin especially given the high productivity of upwelled margin
490 waters. The apparent disconnect between Ga and Al removal in these margin waters might be
491 explained by low Ga water advected from elsewhere, instead of biological scavenging, as

discussed earlier. Below, we also examine possible causes for the lack of Al removal in these Peru margin waters including: a) lack of apparent Al removal due to an additional source of Al and b) lack of Al removal reflecting its physical-chemical speciation. First, there is a small increase in dAl (~1–2 nmol/kg) with depth at these stations along with a large increase in pAl (Lee et al., 2018), suggesting that there could be a source of Al from the margin sediments. Second, previous studies found that dAl is potentially present in the colloidal fraction as organic complexes and/or inorganic precipitates (Perdue et al., 1976; Hydes and Liss, 1977; Sholkovitz, 1978; Tipping et al., 2002). Buck et al. (2018) found low concentrations of dissolved organic carbon in shelf waters of the EPZT, implying only limited formation of Al-organic complexes. If the very low dAl in surface waters of the EPZT is thus mainly inorganic colloids, then perhaps these colloids are less available for biological removal.

A previous study found that surface water Ga/Al ratios correlated with chlorophyll concentrations in the northwest Pacific Ocean (Shiller and Bairamadgi, 2006). They proposed that if this relationship is valid in most surface waters, that one could then use Ga or Chl *a* to adjust the surface ocean dAl residence time in Al-based models of global dust deposition. Here, we examine the variation in surface water Ga/Al ratios and further look into the relationship between this ratio and total Chl *a* in the EPZT. Surface water Ga/Al ratios ranged from 4–9 mmol/mol near the Peru coast (Stns. 1–5). Beyond the upwelling region, Ga/Al ratios increased to a range of 8–13 mmol/mol (Stns. 10–36). Note that a constantly low surface Al and a gradient of surface water Ga were observed in our section (Fig. 5), indicating the variation of Ga/Al ratios in surface waters was regulated by the surface water Ga gradient. High and variable surface water Ga/Al ratios in our Eastern Tropical Pacific section contrast with the low and more constant Ga/Al ratios (0.9–1.7) in the North Atlantic Ocean (Shiller et al., 2014; Measures et al., 2015) and suggest two possibilities: (a) the input is a more important factor than the removal in a low dust deposition area; (b) a residence time effect. That is, in a low dust deposition region, very low Al input results in a high and variable Ga/Al ratio which de-emphasizes the importance of preferential Al scavenging on this ratio. Additionally, if other factors are constant, then the Ga/Al ratio will be proportional to the Ga residence time (Shiller, 1988).

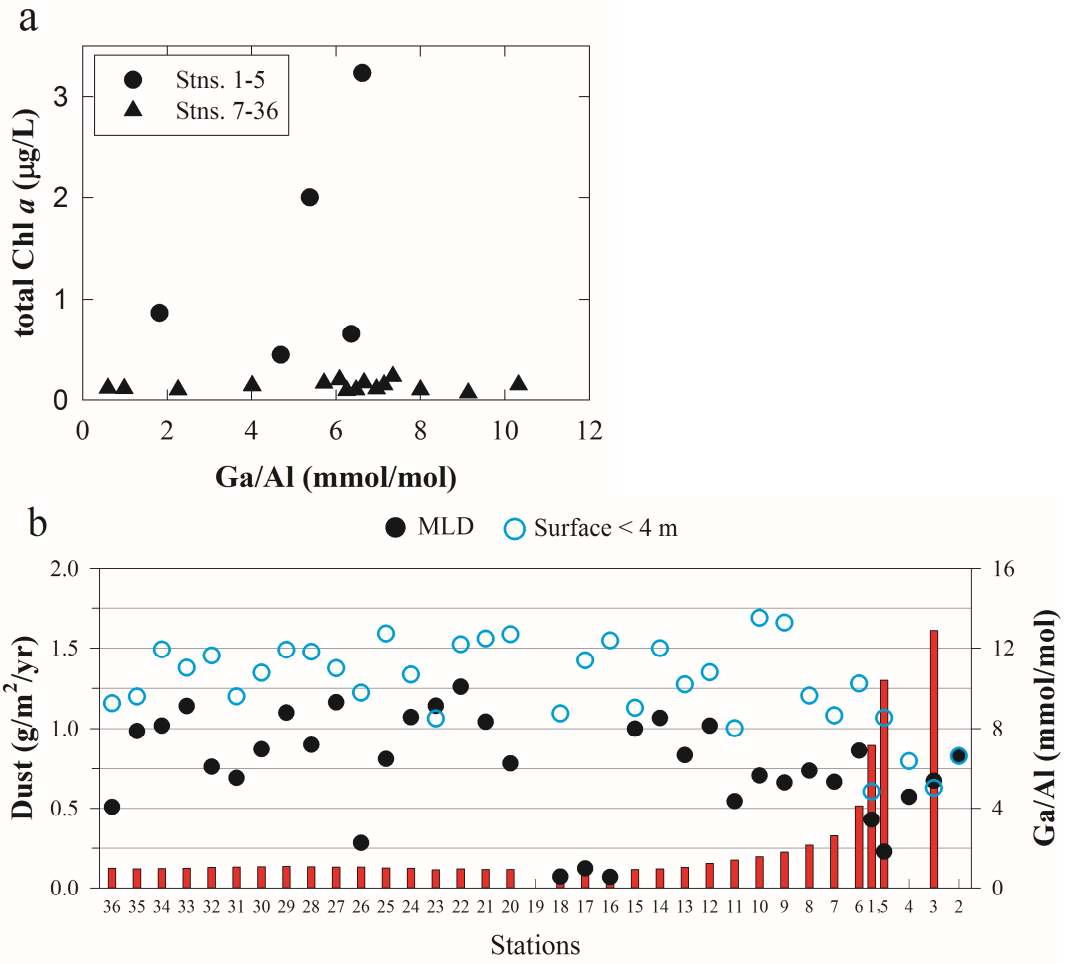

Figure 8. (a) The relationship between the dissolved Ga/Al ratio and total Chl a concentration in surface waters. Note that Ga/Al ratios and total Chl *a* shown in this graph are average concentrations in the mixed layer. (b) Modeled dust deposition (Mahowald et al., 2005) at our sampling stations are shown in red bars. The variations of surface Ga/Al ratios (open circle) and mixed layer Ga/Al ratios (solid circle) in the EPZT.

This relationship between Ga/Al ratios and total Chl *a* concentrations was absent in surface waters in the Eastern Tropical Pacific Ocean (Fig. 8a). Since particulate phosphorus (pP) can be an indicator for biomass abundance as well, we examined the relationship between pP (Ohnemus et al., 2017) and Ga/Al ratios in surface water. We found no apparent correlation between Ga/Al ratios and pP in surface waters. The lack of correlation between surface Ga/Al ratios with total Chl *a* and pP in our section implies that limited Al input results in the variation of surface water Ga/Al ratios here. Amounts of dust deposition to the ocean can affect the Ga/Al

ratios as well. We used the modeled dust deposition (Mahowald et al., 2005) to look at the correlation between dust deposition and surface water Ga/Al ratios (Fig. 8b). It seems the variation of surface Ga/Al ratios is not associated with the dust deposition. Although there is no significant correlation between surface Ga/Al ratios with biogenic indicators and dust deposition across the EPZT, the Ga/Al ratio in coastal waters increased toward the pelagic region, suggesting a) the effect of higher dust input and more intense particle scavenging near the Peru coast relative to open ocean waters and b) a longer residence time beyond the coastal region. In spite of the absence of a linear Ga/Al ratio-Chl *a* correlation from our results, to some extent, the variation of surface water Ga/Al ratios somehow provides insights on the dust deposition estimates on a global (or intra-basin) scale and a changing residence time of mixed layer dAl away from high dust deposition regions.

3.2.2 Ga and Al between subsurface and intermediate water ($\sigma_0 \leq 27.72$ kg m^{-3})

The dissolved Ga and Al distributions from the near surface through the intermediate waters show several interesting features (Fig. 9). First, in the offshore part of the transect beyond the coastal upwelling, there is no evidence of Ga removal associated with the Chl *a* maximum, in accord both with previous observations elsewhere as well as the presumed limited reactivity of Ga relative to other strongly hydrolyzed elements. Similarly, we did not observe a minimum in Al associated with the Chl *a* maximum such as that seen in the Atlantic Ocean (Kramer et al., 2004; Dammshäuser et al., 2013). This suggests that the removal of Al and Ga by biological scavenging is not significant in the oligotrophic gyre waters in the EPZT, consistent both with the oligotrophic nature of these waters and the low dust input.

Next, in general correspondence with the westward increase in surface dissolved Ga, there is an expanding shallow pool (< 200 m) of Ga-enriched water starting around 105°W (Stn. 15/16; Fig. 9a) and roughly corresponding to the waters above the $\sigma_0 = 24.8$ kg m^{-3} isopycnal, which might be classified as waters of the South Pacific gyre. Interestingly, dissolved Al shows no such gyral enrichment pool. However, a very obvious high Al patch was observed in the upper 200 m at three stations from 106°–113°W (Stns. 16–18), which we discuss below. We suspect, therefore, that the Ga-enriched pool of gyre water reflects slow accumulation of Ga within gyre surface waters; i.e., a residence time effect (Shiller, 1998).

Below the Ga-enriched pool, there is a dissolved Ga minimum centered within the nutricline, that outcrops in the vicinity of 90°W (Fig. 9a). This is at shallower depths than the intermediate water Ga minimum observed in other basins (e.g., 500–1000 m; Orians and Bruland, 1988a, b; Shiller, 1998; Shiller and Bairamadgi, 2006) and which appears to be related to advective transport of Ga-depleted waters from high latitude. The minimum starts above the upper boundary of the Peters et al. (2018) water mass analysis, so it is problematic to use the water mass analysis to interpret this feature. One possibility is that the minimum is simply the result of advectively-transported low Ga water being sandwiched between the Ga-enriched near surface pool and the higher Ga waters deeper in the thermocline. Alternatively, the Ga minimum may reflect scavenging removal in the mesopelagic realm. Indeed, Hawco et al. (2016) recently suggested that scavenging of Co onto Mn oxides in the mesopelagic plays a major role in the oceanic Co distribution and the EPZT particulate data (Lam et al., 2018). However, as is discussed below (Section 3.3.1), we did not observe evidence of scavenging removal of Ga in the hydrothermal plume where particulate Mn oxides are even more prevalent.

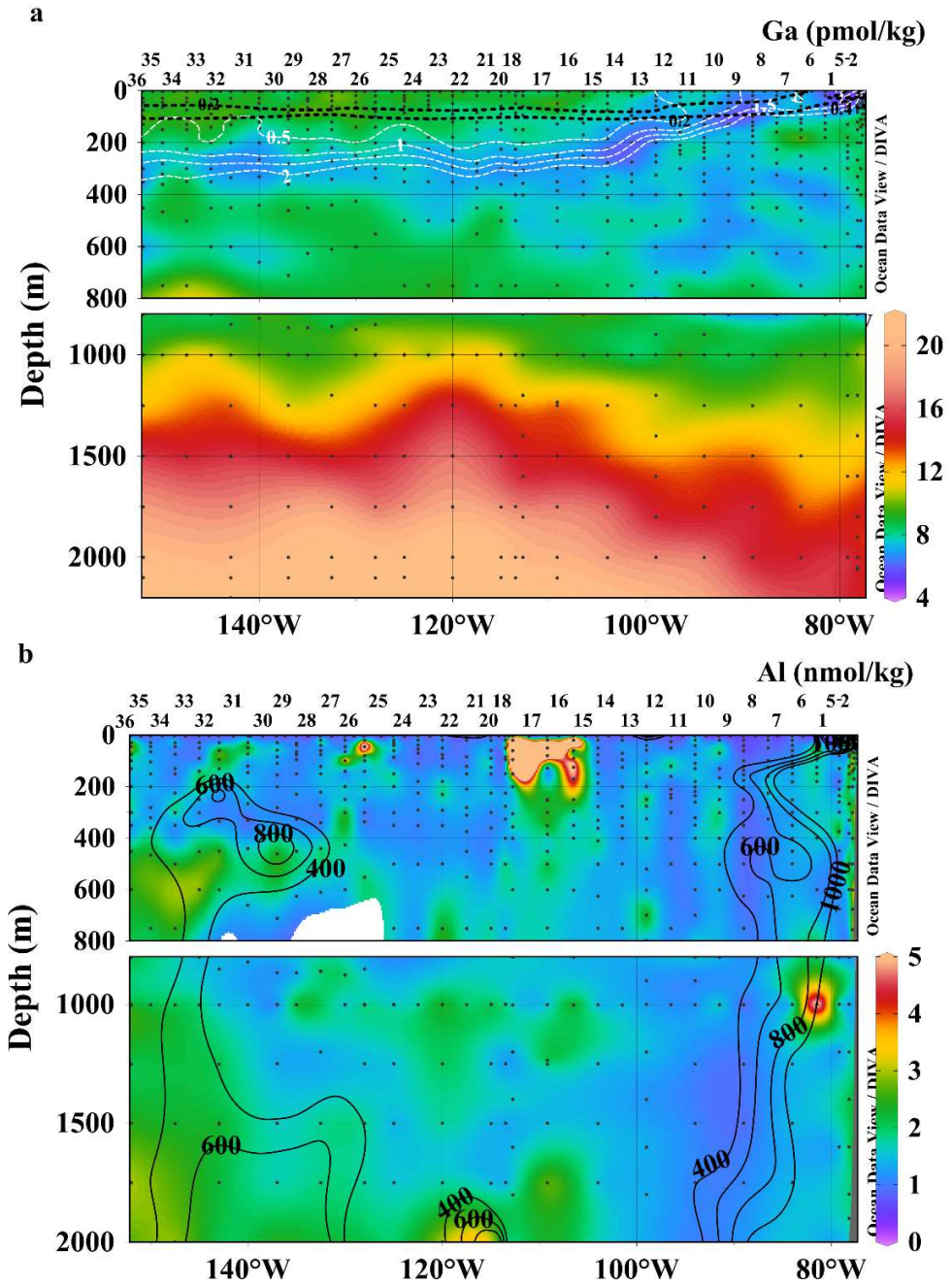

Figure 9. The distributions of dissolved (a) Ga and (b) Al in the upper 2000 m of the water column along the EPZT. Black dashed lines (a) show the Chl *a* (μg/L) maxima. White dashed lines (a) show PO_4 (μmol/kg) contours. Black solid lines (b) show the small sized fraction of pAl (pM) contours.

587 The distribution of dAl showed generally little variability in the upper 1000 m of the
588 water column across the EPZT (Fig. 9b). However, several exceptions to this were observed,
589 specifically: subsurface water at Stns.16–18, water at 400–2000 m depth at Stns. 32–36, and
590 water near the Peru margin. We discuss these areas below.

591 The small patch of highly dissolved Al-enriched water in the upper 200 m in the middle
592 of the section (Stns. 16–18) is a distinct and unusual feature of the section that does not appear
593 to be an artifact of contamination. Sampling tests, including touching open bottle tops to gloves
594 and spigots, revealed no measurable contamination. Samples (n = 221) in the upper 1000 m for
595 stations 7 to 23 (excluding the upper 200 m at Stns. 16, 17, and 18) have an average
596 concentration of 1.5 ± 0.4 nM. This indicates that the sample bottles, processing, and analysis
597 were unlikely sources of the elevated signals. In addition, the same GoFlo bottles were used for
598 the deep casts at these stations and showed no similar artifacts. Also, the first two Al-enriched
599 stations occurred before the hydrothermal plume was sampled and thus the bottles would not
600 have been exposed to the Al-enriched hydrothermal waters. We thus tentatively accept these
601 elevated near-surface results as valid, but make only a limited interpretation here. We note first
602 that other dust-derived elements, such as Ga and Fe, do not show a dissolved enrichment in these
603 waters, nor is there an enrichment in particulate Al or Fe (Lee et al., 2018), nor in Chl *a*.
604 However, John et al. (2018) do show a similar small patch of high δ^{56}Fe water at the same place.
605 This high δ^{56}Fe is compatible with dust input. We speculate that there had been a brief dust event
606 that resulted in rapid biological Fe uptake from these oligotrophic waters and which left the Al
607 and δ^{56}Fe as the only evidence of the event. A rapid response of surface water dissolved Al to
608 dust input has been observed before in the Sargasso Sea (Jickells et al., 1994) as well as in
609 mesocosm experiments (Wuttig et al., 2013). The oligotrophic nature of these waters may also
610 limit the rate of scavenging removal of dAl. Furthermore, at least in the North Pacific near
611 Midway Island, dust input to surface waters has been shown to be highly episodic with the
612 annual total being delivered in just a few events (Donaghay et al., 1991). That said, our observed
613 enrichment of ~15 nmol/kg over ~75 m of water column would require a dust deposition event
614 on the order of 7.5 g dust m^{-2} (assuming crustal Al composition and 5% Al solubility) to cause
615 the observed dAl enrichment. This is on the order of the total annual deposition to the dustiest
616 areas of the North Atlantic and far higher than the estimated annual deposition for this region of
617 the South Pacific (e.g., Han et al., 2008). Clearly, we are left with a conundrum.

Near the Peru margin, slightly elevated dAl was observed ~20–100 m below the surface east of Stn. 9 (Fig. 9b), corresponding with increased total pAl (small + large fractions) (Lee et al., 2018). Higher lithogenic particulate materials were seen in the coastal upwelling region which was a result of dust deposition and lateral advection from shelf sediments (Lam et al., 2018). Anomalies in various chemical properties in the mid-depth range along the continental slope include relatively high dissolved Fe (Resing et al., 2015; John et al., 2018), $d^{232}Th$ (Schlitzer et al., 2018) and ^{228}Ra (Sanial et al., 2018), as well as the highest lithogenic material concentration at a slope station (Stn. 5; Lam et al., 2018) suggesting a potential source of dAl from the margin. In other words, the slight increase in dAl in Peru margin waters suggests a mechanism of increased dust input (relative to the rest of the section) along with scavenging removal in productive upwelled waters followed by sinking and remineralization of dAl from sinking particles and margin sediments. In contrast, there was no evidence of Al release from shelf/margin sediments off the northwest African coast (Measures et al., 2015) although many lithogenic material tracers (e.g., $d^{232}Th$, dissolved Fe) also showed a source from sediments there (Hatta et al., 2015; Revels et al., 2015). Furthermore, previous work has shown variable Al solubility in aerosols from different dust sources (Baker et al., 2006; Shelley et al., 2018) as well as a function of the dust load (Shelley et al., 2018).

Above, in our description of the apparent non-conservative Ga distribution (Fig. 2c), we mentioned that Ga removal was commonly observed in the intermediate waters, especially near the Peru margin. This is opposite from the observation of slightly increased Al in these waters (see above), which raises the question of why Ga and Al have contrasting behaviors in intermediate waters. We rule out the possibility of this being an artifact of our Ga endmember selection for the conservative distribution. First, we note that the depth of the most depleted Ga does not coincide with the contour of any particular water type. The most depleted mid-depth Ga appears to be on the first half of the transect (mostly at Stns. 1–15). We thus examined the relationship between dissolved Ga and salinity in the intermediate layers (27 kg m^{-3} < $\sigma_0 \leq$ 27.72 kg m^{-3}) at Stns. 1–15 to evaluate the role of a simple mixing between different water masses in these waters. Briefly, the composition of water masses in the intermediate layer at Stns. 1–15 mainly included EqPIW, AAIW and PDW, while UCDW was a minor component (range: 0–34 %; average: 6%; median: 0%; the most UCDW influenced waters are below 1500 m at Stns. 13 and 15 where less Ga depletion was seen) (Peters et al., 2018). Note that Ga endmember

estimates for UCDW are not very different from those in other intermediate water masses (Table 1). Thus, the influence of the UCDW fractions must be limited in these Ga-depleted samples. At these stations (Stns. 1–15), in the upper intermediate layer (500–1000 m), a combined fraction of EqPIW and AAIW accounts for more than 50 % of the water. Below 1000 m, PDW becomes a dominant water mass (Peters et al., 2018). Fig. 10 shows dissolved Ga versus salinity of intermediate water samples below 1000 m depth at Stns. 1–15 in which the pronounced Ga anomaly can be seen. If we assumed these waters at 1000 m represent the mixture of EqPIW and AAIW, a linear mixing trend between the EqPIW-AAIW mixture and PDW can be drawn. We find that Ga, in many samples, falls below this mixing trend, suggesting intermediate water Ga removal near the Peru margin is not an artifact. However, it is unclear why we did not see a stronger removal for Al in these waters.

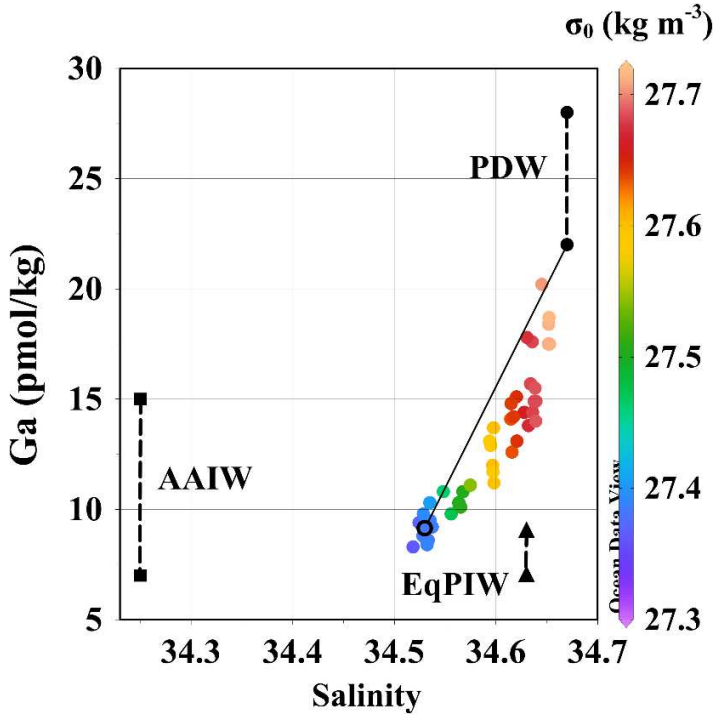

Figure 10. Dissolved Ga versus salinity in the range of 27.3 kg m^{-3} < $\sigma_0 \leq$ 27.72 kg m^{-3} (approximately 1000-2250 m) at Stns. 1–15. A purple circle with black outline represents an average from all samples of 1000 m at Stns. 1–15. Black circles show the range of Ga endmember values for PDW. Triangles and squares show a range of Ga endmembers in EqPIW and AAIW, respectively. Black solid line is a mixing trend between an average value of 1000 m samples and a low-Ga PDW endmember (22 pmol/kg).

Increased dAl (> 2 nmol/kg) at 400–2000 m at Stns. 32–36 partially overlapped with slightly elevated pAl (Fig. 9b) (Lam et al., 2018; Lee et al., 2018). Since the distributions of dAl and pAl respond at different time scales, the lack of complete overlap of their distributions is not exceptional. Dissolved Al samples represent a decadal time-scale while pAl responds on a time scale of weeks to months in the water column. In other words, particulate samples show a relatively instant picture compared to dissolved samples. It is surprising, however, that this dAl enrichment on the western, open ocean boundary of the EPZT section is more prominent than the dAl enrichment observed along the Peru margin. This may result from greater biological removal along the margin as well as different sources of the Al. For instance, Lam et al. (2018) pointed out that lateral inputs of lithogenic particles from volcanic islands (i.e., Marquesas Islands and Tuamotu Archipelago) and submarine plateaus (i.e., Tuamotu Plateau) in the upper 2000 m of the western part of the transect could be potential sources for lithogenic materials in this region. Furthermore, previous work has shown variable Al solubility in aerosols relating to differing dust loads and dust (Baker et al., 2006; Shelley et al., 2018).

3.3 Ga and Al in the deep and bottom water (σ_0 > 27.72 kg m^{-3})

Deep water dissolved Ga and Al in the EPZT ranges from 19–35 pmol/kg and 1–12 nmol/kg, respectively. This is lower than the concentration range of both elements in the deep Atlantic Ocean which is influenced by the Al- and Ga-rich NADW (Measures and Edmond, 1990; Measures, 1995; Shiller, 1998; Shiller and Bairamadgi, 2006; Measures et al., 2015; Middag et al., 2015). Excluding the area influenced by the EPR hydrothermal plume, low Al (generally < 4 nmol/kg) in deep water is in agreement with the range of Al previously reported in deep North Pacific, Indian and Southern Oceans (Orians and Bruland, 1986; Obata et al., 2004; Middag et al., 2011). Compared with deep water Ga (12–30 pmol/kg) in the North Pacific (Orians and Bruland, 1988a; Shiller and Bairamadgi, 2006), the slight increase in deep water Ga in our section might be caused by the accumulation of Ga during the southward flow of PDW (Peters et al., 2018) and/or from local sediment inputs.

Various interesting features in deep water dissolved Ga and Al distributions were observed in the EPZT. Elevated deep water Ga and Al concentrations were commonly observed

696 in this section, relative to the rest of water column First, the high Al concentrations across the
697 deep waters are abruptly interrupted at Stn. 15 (~930 km east of the EPR) where bottom water Al
698 concentrations are relatively low at this station compared with most deep waters in the transect.
699 Third, at the westernmost part of the transect (Stns. 32 and 36), dissolved Ga decreased and dAl
700 increased toward the bottom, respectively. Based on the results of OMPA, the influence of
701 AABW is most pronounced in these western deep waters, relative to deep waters in the rest of
702 section (Peters et al., 2018). Lastly, the two most striking EPZT deep water features for Ga and
703 Al are the enrichments in these elements in the hydrothermal plumes and nepheloid layers. We
704 discuss these features further in the next two sections below.

705 3.3.1 Ga and Al in the EPR hydrothermal plumes

706 A remarkable extended hydrothermal plume, ranging from the EPR at Stn. 18 westward
707 for thousands of kilometers was previously reported for this section (Resing et al., 2015) and our
708 Al data was originally reported therein. The dissolved Ga section (Fig. 2a) suggests that Ga is
709 likewise affected by hydrothermal input. However, the extent of Ga enrichment is somewhat
710 obscured by the fact that waters east of the EPR (which were not observed to be hydrothermally
711 influenced; Resing et al., 2015) are also high in dissolved Ga and show a similar "excess"
712 dissolved Ga (Fig. S4). In contrast, increased dAl (up to 12 nmol/kg at Stn. 18, 2625 m) in the
713 hydrothermal plumes clearly extended westward ~3000 km in the EPZT (Fig. 2b), and this was
714 also seen in other dissolved trace elements (Fe, Mn) (Resing et al., 2015; Fitzsimmons et al.,
715 2017) and $^{3}He_{ex}$ (Jenkins et al., 2018). Increased dAl has been observed in the hydrothermal
716 plume in the MAR as well (Lunel et al., 1990; Measures et al., 2015). Higher hydrothermal dAl
717 in the MAR plume than in the southern EPR is thought to be due to the effect of the axial valley
718 of the MAR (Resing et al., 2015) in that axial rift-valley walls in the MAR confine the
719 movement of buoyant hydrothermal plumes. Resing et al. (2015) inferred that the larger dAl
720 source from hydrothermal vents along the southern EPR caused the extended dAl plume seen in
721 the far field. More active eruptions on the sea floor in the southern EPR (Gamo et al., 1993)
722 could be a possible source for dAl in the southern EPR hydrothermal plume, as proposed by
723 Resing et al. (2015).

724 In Figures 11a and b, we show the integrated inventories of dissolved Ga and Al in the
725 depth range of the hydrothermal plume plotted versus the inventory of excess ^{3}He (from Jenkins

et al., 2018). The depth range of the integration was nominally 2200 – 2800 m, though for Stn 18 the bottom of the profile was at only 2640 m. This diagram shows several interesting things: a) Stn. 18 at the ridge crest falls on a different trend, in agreement with the suggestion (Resing et al., 2015; Jenkins et al., 2018) that the extended hydrothermal plume is actually sourced from elsewhere on the EPR; b) for the other stations, the Ga and Al trends versus $^{3}He_{ex}$ are linear, suggesting conservative dilution of these elements within the extended plume; and, c) there is a far greater relative change in Al than Ga.

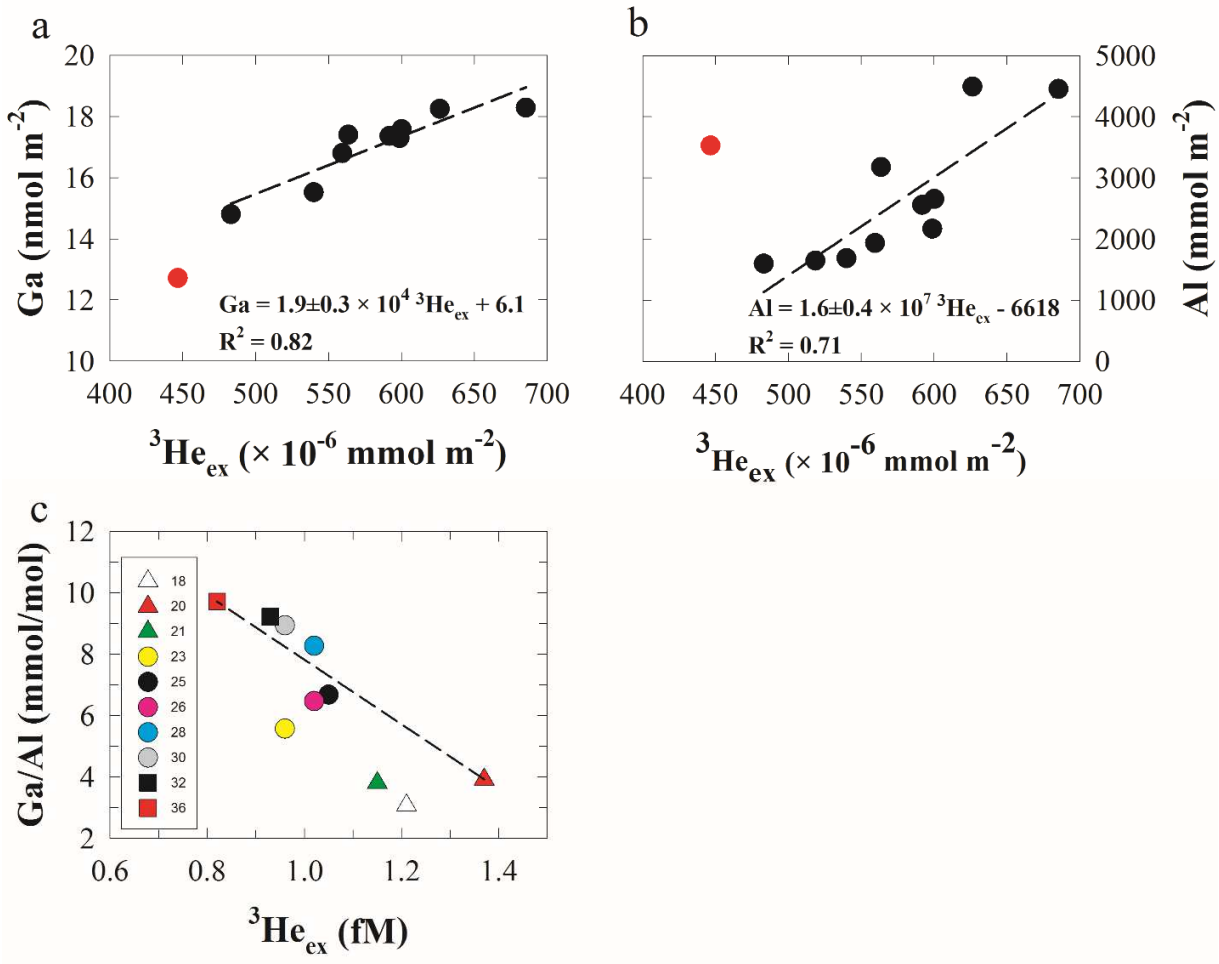

Figure 11. The integrated inventories of dissolved (a) Ga and (b) Al with $^{3}He_{ex}$, within a depth range of 2200-2800 m west of the EPR. Note that at Stn 18 (red circles in a & b) the integration range extended only to the bottom depth of 2640 m. Black circles are integrated Ga, Al and $^{3}He_{ex}$ concentrations at Stns. 20–36. (c) The relationship between Ga/Al ratio and $^{3}He_{ex}$ at 2500 m, west of the EPR. The dashed line represents simple mixing between Stn. 20 and Stn. 36. Note abnormally low $^{3}He_{ex}$ at Stn. 18.

741 Earlier (Section 3.2.2), we suggested the possibility of Ga scavenging by Mn oxides in
742 the subsurface Ga minimum. In the hydrothermal plumes, however, the dissolved Ga
743 concentration is largely controlled by dilution. There is no evidence of Ga or Al scavenging by
744 hydrothermal particles in our section. That is, there is no correspondence of depleted Ga (or Al)
745 and increased Mn oxides in the hydrothermal plumes. Thus, Ga and Al scavenging appears to be
746 limited and fairly slow and the particulate Ga and Al enrichments in these hydrothermal particles
747 are suppressed by highly enriched particulate Mn and Fe concentrations. This would seem to rule
748 out mid-depth Ga scavenging by Mn oxides unless the structure of Mn oxides in subsurface
749 waters is significantly different from those in the hydrothermal Mn oxides and thus has a very
750 different ability for Ga scavenging.

751 We can also examine the variation of dissolved Ga/Al ratios in these hydrothermally
752 influenced waters. A decreased Ga/Al ratio was observed in the hydrothermal plume, compared
753 with the Ga/Al ratio in ambient deep water (Fig. 4). Low dissolved Ga/Al ratios would be
754 expected close to the ridge crest due to the dissolution of basalt under acidic, high-temperature
755 conditions and since the crustal Ga/Al ratio (0.084 mmol/mol; Rudick and Guo, 2014) is low
756 compared to seawater. Since a mid-depth (~2500 m) hydrothermal ^{3}He tongue was observed in
757 the EPR and extending westward ~4000 km (Resing et al., 2015; Jenkins et al., 2018), we focus
758 on the variation of Ga/Al ratios at 2500 m on west of the EPR (Fig. 10c). An inverse correlation
759 between the Ga/Al ratio and $^{3}He_{ex}$ in hydrothermal plume waters, along with the positive linear
760 correlations between each of the two elements and $^{3}He_{ex}$, suggests this is a result of simple
761 mixing between high (Stn. 36) and low (Stn. 20) Ga/Al ratios endmembers. Lee et al. (2018) do
762 note slightly increased pAl near the ridge crest, so there is at least some limited scavenging of Al
763 on hydrothermal particles. But, overall, the behavior of dissolved Ga and Al in the EPR extended
764 hydrothermal plumes is dominated by dilution.

765 We can make an estimate of the global hydrothermal Ga flux by using the slope of the
766 Ga-$^{3}He_{ex}$ linear regression ($1.9\pm0.3 \times 10^{4}$ mol Ga/ mol $^{3}He_{ex}$) and the global ^{3}He hydrothermal
767 flux (450±50 mol/yr, Schlitzer, 2016). This results in a global dissolved Ga flux from
768 hydrothermal activity of $8.6\pm1.7 \times 10^{6}$ mol/yr, 2–7 times higher than a hydrothermal Ga flux
769 estimate ($1.4–3.8 \times 10^{6}$ mol/yr) derived from Ga concentrations in various hydrothermal fluids
770 (Metz and Trefry, 2000) and a high-temperature hydrothermal water flux of $5.6\pm0.6 \times 10^{13}$ kg/yr

771 (Elderfield and Schultz, 1996; Mottl, 2003; German and Seyfried, 2014). Applying the same
772 method to dAl (i.e., a slope of 1.6±0.4 × 10^7 mol Al/mol $^3He_{ex}$), we estimate a global
773 hydrothermal dAl flux of 7.2±2.0 × 10^9 mol/yr, which is an order of magnitude higher than
774 previous reports (axial high temperature fluxes: 1.2–6 × 10^8 mol/yr, Elderfield and Schultz,
775 1996).

776 We can compare these estimates of hydrothermal Ga and Al input with estimates of their
777 aeolian and fluvial inputs. For Al, the aeolian source of dAl can be derived from global dust
778 deposition (450 Tg/yr; Jickells et al., 2005) with 8% Al in the UCC (Rudick and Guo, 2014) and
779 Al solubility of 5% (Measures et al., 2010). This yields a dAl input from dust dissolution in the
780 surface ocean 6.7 × 10^{10} mol/yr. Gaillardet et al. (2014) estimated the fluvial flux of dAl to be
781 4.0 × 10^{10} mol/yr, though the actual flux to the ocean is likely much lower due to estuarine
782 removal of colloidal/organic fluvial Al.

783 For Ga, there is a lack of reported solubility from aerosol/dust samples. We thus estimate
784 a likely range for aeolian Ga input by choosing a probable range in Ga/Al input ratios. We can
785 choose a low Ga/Al input ratio of 0.1 mmol/mol based on both crustal Ga/Al ratios and ratios
786 from uncontaminated streams (Shiller, 1988; Shiller and Frilot, 1996). Likewise, we can choose
787 a high estimate of 1 mmol/mol from dissolved Ga/Al ratios in surface waters of high dust input
788 regions of the North Atlantic (Shiller, 1988; Shiller et al., 2014). With the aeolian dAl input, this
789 yields a probable input range of 7–70 × 10^6 mol/yr Ga from dust dissolution. For rivers, the
790 review of Gaillardet et al. (2014) suggests a fluvial dissolved Ga input of 1.4 × 10^7 mol/yr. Here
791 again, this ignores likely estuarine removal of Ga (McAlister and Orians, 2012) and may also be
792 biased high due to inclusion of some unusually high Ga rivers in the fluival average.

793 While our estimates above are crude, they nonetheless both emphasize that hydrothermal
794 input of Al is likely to be of local, not global importance and also restate the overall importance
795 of aeolian inputs for Al to the ocean. For Ga, the hydrothermal flux estimate is comparable to the
796 low end of aeolian Ga flux which suggests the contribution of hydrothermal Ga input to the
797 oceanic inventory might be important. Note that previous studies showed variable Al/$^3He_{ex}$ ratios
798 in different hydrothermal systems (Jenkins et al., 2015; Measures et al., 2015; Resing et al.,
799 2015). This probably results in the higher hydrothermal Al flux estimates derived from the

800 $Al/^{3}He_{ex}$ ratio in the EPR than previously reported for global hydrothermal Al flux estimates.
801 Thus, the EPR data likely overestimates the global impact of hydrothermal input for Ga and Al.

802

803 3.3.2 Ga and Al in the bottom nepheloid layer

804 Although Ga profiles showed no increase in bottom waters at most stations (Fig. 2a), the
805 difference between observed and conservative Ga suggests that dissolved Ga has additional
806 inputs to the bottom waters, with the exception of the westernmost part of the section (Stns. 32–
807 36) (Fig. S4). There are two possible explanations for why near bottom waters at Stns. 32–36 do
808 not show the apparent Ga input that other bottom waters in the section do. We note first that the
809 bottom waters at Stns. 32–36 were the only waters in the section having a significant AABW
810 component and they also had a significant LCDW component rather than being dominantly
811 PDW. It is possible that the PDW in the EPZT shows more apparent Ga input than
812 AABW/LCDW due to its longer transit/exposure to bottom inputs. Alternatively (or
813 additionally), it is possible that we overestimated the endmember Ga concentrations of AABW
814 and/or LCDW. Indeed, while Shiller and Bairamadgi (2006) provided the 25–30 pmol/kg
815 estimate for AABW used here, Shiller (1998) suggested an AABW Ga concentration < 17
816 pmol/kg. For Al, its concentration increased from 4.2 to 5.6 nmol/kg below 4,000 m depth at
817 Stns. 32–36. In the South Atlantic basin, Middag et al. (2015) observed fairly low Al in the
818 AABW (mostly < 2 nmol/kg), with slightly increased Al (but still < 5 nmol/kg) near the bottom.
819 Thus, the increased bottom water dAl at Stns. 32 and 36 is likely an indication of Al
820 accumulation (either by remineralization of sinking particles or from sediment resuspension)
821 during the northward transit of AABW.

822 For most of bottom waters, higher observed than conservative Ga in bottom water
823 suggests additional Ga inputs from sediment resuspension and accumulated Ga during advection.
824 There was also increased dAl in the bottom water across the transect. Previous studies have
825 observed elevated dAl in bottom waters elsewhere and attributed this to input from sediment
826 resuspension (Moran and Moore, 1991; Measures et al., 2015). Benthic nepheloid layers were
827 generally observed ranging 600–750 m above the bottom at Stns. 1, 6–36 (Ohnemus et al., 2018).
828 Dissolved ^{232}Th also showed increases in bottom waters (Pavia et al., 2018). All these
829 observations imply a source of dissolved Ga and Al in the bottom waters in the EPZT from

resuspended sediments. Furthermore, the dissolved Ga/Al ratio (Fig. 4) in these bottom waters is generally lower than the waters above. Given that other sources of Ga and Al (i.e., aeolian, fluvial, and hydrothermal) tend to show comparatively low Ga/Al ratios, this bottom decrease in the ratio is also compatible with the idea of benthic input of these two elements, though certainly the decrease in the ratio could be accomplished with just an Al input.

In contrast to the near-bottom increase observed (Al) or inferred (Ga) for most of the section, there was slightly decreased dissolved Al in the bottom waters at Stn. 15, relative to deep waters in the rest of transect (Figs. 2 and 3). This is puzzling given the near-bottom increase in suspended particulate matter for this station (Ohnemus et al., 2018). For instance, particulate trace element data showed that benthic nepheloid layer particles (mostly present in small size fraction) at Stns. 13–17 were characterized with low pAl, pTi and pFe but high pFe/pAl and pMn/pAl ratios (Lam et al., 2018; Lee et al., 2018). These samples also showed significant excess Fe and Mn (oxyhydr)oxides near the bottom, suggesting these benthic particles were associated with hydrothermal particles (Lam et al., 2018; Lee et al., 2018). Lee et al. (2018) suggested that hydrothermal particles could be delivered from the nearby Bauer Basin (see Fig. 1) where ferromanganese sediments have been found and are likely transported by eastward bottom currents from the ridge crest of the EPR through transform fault troughs (3°–5° S) (Lonsdale, 1976; Reid, 1997). The GP16 OMPA results showed that PDW accounted for up to 70% of deep water samples at Stns. 13–17, suggesting mainly southward flow in this region (Peters et al., 2018). Thus, it is possible that fine ferromanganese materials were carried by southward flows from the Bauer Basin to these stations (Stns. 13–17). Lee et al. (2018) also suggested that additional sources of the excess pFe and pMn in small size fractions at Stns. 13–17 could be hydrothermal particles derived from low temperature hydrothermal activity in the Bauer and Peru Basins (McMurtry and Burnett, 1975; Marchig et al., 1999). As mentioned above (Section 3.3.1), dAl and Ga mainly show dilution in the hydrothermal plume, suggesting limited Al and Ga scavenging by hydrothermal particles (Fe and Mn (oxyhydr)oxides). Thus, the low Al content in the hydrothermal particles is unlikely to supply a significant dissolution of Al and/or Al-rich porewater (or Ga) from sediment resuspension. However, the observation of increased dissolved $^{231}Pa/^{230}Th$ ratios at these stations below 3000 m (Pavia et al., 2018) is likely caused by suspended particles preferentially scavenging of dissolved ^{230}Th relative to dissolved ^{231}Pa (Anderson et al., 1983; Hayes et al., 2015). This implies a higher affinity of ^{230}Th and ^{231}Pa onto

861 Fe and Mn oxyhydroxides than that of Ga and Al. This is accord with the greater first hydrolysis
862 constant of Th(IV) than those of Ga(III) and Al(III) (Stumm and Morgan, 1996).

863 We also note, however, that the high fraction of PDW in the bottom waters at Stns. 13–17
864 (Peters et al., 2018) and the comparatively low Ga and Al in PDW (e.g., waters at ~2500 m along
865 the Peru margin are dominantly PDW; see Figs. 2 and 3) suggests another contribution to the low
866 near bottom Al at Stn. 15. That is, the advection of low-Ga and low-Al PDW by southward
867 bottom currents (Reid, 1997; Peters et al., 2018) should result in lower Ga and Al at stations east
868 of the EPR.

869 *3.4 The relationship of Al and Silica*

870 A well-correlated Al-Si relationship was observed in the Arctic and North Atlantic
871 Oceans (Middag et al. , 2009, 2011), suggesting release of Si and Al from the remineralization of
872 biogenic particles. However, the breakdown of this correlation in other oceanic regions (Hydes,
873 1979; Stoffyn and Mackenzie, 1982; Measures et al., 2015) argues that the remineralization of
874 Si-phase particle is not a factor of increased Al in the water column. In our dataset, we didn't
875 observe an Al-Si correlation, in agreement with previous observations in the central North
876 Pacific Ocean (Orians and Bruland, 1985) and implying that Al is not significantly released from
877 those biogenic particles. Middag et al. (2015) suggested that the absence of the positive Al-Si
878 correlations could be caused by the influence of old water masses having high Si and low Al, and
879 a decreased Al/Si ratio in diatom opal due to very low Al in surface waters (Collier and Edmond,
880 1984).

881

882 **4. Conclusions**

883 Here we have reported high-resolution dissolved Al and Ga distributions in the Eastern
884 Tropical South Pacific Ocean. Key features that were observed in this section include: a)
885 relatively low dissolved Ga and Al concentrations at the surface; b) a noticeable dissolved Al and
886 Ga input from the hydrothermal plumes; and, c) a bottom source of deep water Al and Ga from
887 sediment resuspension.

In the surface water, there was relatively low dissolved Ga and Al with high and variable Ga/Al ratios across the transect, as compared with previously reported values in the North Atlantic Ocean. This suggests that low dust input and increased residence times due to the oligotrophic nature of the gyre waters affect these elements in the Eastern Tropical South Pacific Ocean. Surprisingly, no significant dAl removal was observed in upwelled coastal surface waters. A gradient of Ga was observed in surface water with increasing concentration towards the open ocean, but not in dAl. Possible reasons for this observation include: (1) additional dAl inputs from shelf sediments, evidenced by increased pAl (Lee et al., 2018), (2) dissolved Al might be present as inorganic complexes and thus less reactive to scavenging, or (3) the horizontal gradient in surface dissolved Ga is a result of advectively-transported low-Ga water, though from an unidentified origin, instead of biological scavenging. The Al in the surface water shows a similar pattern with no large excursions, including at the stations where large subsurface Al concentrations were observed.

Various interesting features of dissolved Ga and Al were observed between surface and intermediate layers. Beyond the coastal upwelling zone, the absence of Ga and Al removal associated with the Chl *a* maximum suggests that the removal of Al and Ga by biological scavenging is not significant in the oligotrophic gyre waters in the EPZT. West of 105°W, an expanding shallow pool (< 200 m) of Ga-enriched water, recognized as South Pacific gyre water, suggests slowly accumulated Ga within the gyre circulation. However, we did not observe dissolved Al enrichment in this Ga-enriched pool. West of 90°W, a dissolved Ga minimum centered within the nutricline, right below the Ga-enriched pool, is coincident with a Mn oxide maximum (Lee et al., 2018). This could be simply the result of the advection of low Ga water or Ga removal by Mn oxides. However, the later explanation seems less likely due to the lack of Ga scavenging in the hydrothermal plume.

Besides the hydrothermal dAl plume, several other regions with elevated dAl were observed in the EPZT: a) subsurface water at Stns.16–18, b) water near the Peru margin, and c) water at 400–2000 m depth at Stns. 32–36. Anomalously high dAl water in the upper 200 m at Stns. 16–18 does not appear to be an artifact of contamination. A similar small patch of high δ^{56}Fe water, compatible with dust input, was observed at the same place (John et al., 2018). We speculate that this observation is resulted from after a brief dust event. Near the Peru margin,

slightly elevated dAl below the surface suggests a potential source of dAl from the margin, evidenced by increased ^{228}Ra, dissolved Fe and other lithogenic elements (pAl, pTi, d^{232}Th) (John et al., 2018; Lam et al., 2018; Lee et al., 2018; Sanial et al., 2018; Schlitzer et al., 2018). Increased dAl (> 2 nmol/kg) was observed at 400–2000 m at Stns. 32–36, partly associated with increased pAl. It is surprising, however, that this dAl enrichment on the western, open ocean boundary of the EPZT section is more prominent than the dAl enrichment observed along the Peru margin. This may result from greater biological removal along the margin as well as different sources of the Al with differing Al solubility. For Ga, a depletion was commonly observed in the intermediate waters, especially near the Peru margin. This is opposite from the observation of slightly increased Al in these waters and still remains to be explained.

Elevated deep water Ga and Al concentrations were commonly observed in this section, relative to the rest of water column. The two most striking EPZT deep water features for Ga and Al are the enrichments in these elements in the hydrothermal plumes and nepheloid layers. However, at Stn. 15, bottom water Al concentrations are relatively low compared with most deep waters in the transect, even in the nepheloid layer. Lee et al. (2018) observed fine hydrothermal particles in these bottom waters at Stns. 15–17 (immediately east of the EPR). We speculate low dAl at Stn. 15 is explained by limited Al dissolution from these resuspended hydrothermal particles and/or the advection of low-Al PDW from north. At the westernmost part of the transect (Stns. 32 and 36), decreased Ga and increased dAl near the bottom indicate AABW influence.

We observed pronounced hydrothermal Al and to a lesser extent hydrothermal Ga signals in the EPZT. We estimated a global hydrothermal flux of dissolved Ga ($8.6\pm1.7 \times 10^6$ mol/yr) and Al ($7.2\pm2.0 \times 10^9$ mol/yr), derived from the slopes of Ga/^{3}He$_{ex}$ and Al/^{3}He$_{ex}$ relationships in the extended EPR plume. Hydrothermal Al flux is an order of magnitude less than aeolian input of Al while hydrothermal Ga flux is comparable to the low end of aeolian Ga flux estimates. We also note that the global hydrothermal Al fluxes estimated from our EPR data are much higher than previous estimates. Within the hydrothermal plumes, relatively low Ga/Al ratios compared to the rest of the transect, suggests a source that is more similar to UCC composition. A linear correlation between Ga/Al ratio and ^{3}He$_{ex}$ indicates preferential Al removal or mixing of low hydrothermal-derived Ga/Al and high Ga/Al in background seawater.

Our study again demonstrates the importance of aeolian inputs and sediment resuspension in dissolved Ga and Al distribution in the ocean. This work also suggests areas of emphasis for future research. Specifically, the speciation (organic, inorganic, and colloidal) of Al at low concentrations may provide further insight to its reactivity. The determination of Ga solubility in dust will be an aid to the application of the surface water Ga/Al ratio. Studies of Ga input from sediments and via estuaries are also needed. Further work on the oceanic Ga distribution will also aid in the application of conservative mixing models to better resolving locations of Ga input and removal.

Acknowledgements

We thank Jim Moffett and Greg Cutter for their successful leadership of this expedition. Many thanks to the supertechs, the staff of the Oceanic Data Facility, and the Captain and crew of the R/V Thomas G. Thompson. We especially thank Missy Gilbert for her analytical skills in our lab. This work was supported by the National Science Foundation grant OCE-1261214 to AMS. JAR was funded by US NSF award OCE-1237011 and NOAA Cooperative Agreement NA15OAR432006. This is JISAO Publication number 2018-0179 and PMEL number XXXX. Data produced under this grant have been submitted to BCO-DMO.

Reference

Anderson, R.F., Bacon, M.P., Brewer, P.G., 1983. Removal of 230Th and 231Pa at ocean margins. Earth Planet. Sci. Lett. 66, 73–90. doi:10.1016/0012-821X(83)90127-9

Bacon, M.P., Anderson, R.F., 1982. Distribution of thorium isotopes between dissolved and particulate forms in the deep sea. J. Geophys. Res. Ocean. 87, 2045–2056. doi:10.1029/JC087iC03p02045

Baker, A.R., Jickells, T.D., Witt, M., Linge, K.L., 2006. Trends in the solubility of iron, aluminium, manganese and phosphorus in aerosol collected over the Atlantic Ocean. Mar. Chem. 98, 43–58. doi:10.1016/j.marchem.2005.06.004

Brown, M.T., Bruland, K.W., 2009. Dissolved and particulate aluminum in the Columbia River and coastal waters of Oregon and Washington: Behavior in near-field and far-field plumes. Estuar. Coast. Shelf Sci. 84, 171–185. doi:10.1016/j.ecss.2009.05.031

Bruland, K.W., 1983. Trace elements in sea water., in: Riley, J.P., Chester, R. (Eds.), Chemical Oceanography. Academic, London, pp. 157–220.

Bruland, K.W., Orians, K.J., Cowen, J.P., 1994. Reactive trace metals in the stratified central North Pacific. Geochim. Cosmochim. Acta 58, 3171–3182. doi:10.1016/0016-7037(94)90044-2

Bruland, K.W., Rue, E.L., Smith, G.J., DiTullio, G.R., 2005. Iron, macronutrients and diatom blooms in the Peru upwelling regime: brown and blue waters of Peru. Mar. Chem. 93, 81–103. doi:10.1016/j.marchem.2004.06.011

Bruland, K.W., Middag, R., Lohan, M.C., 2014. 8.2 - Controls of Trace Metals in Seawater, in: Holland, H.D., Turekian, K.K. (Eds.), Treatise on Geochemistry (Second Edition). Elsevier, Oxford, pp. 19–51. doi:0.1016/B978-0-08-095975-7.00602-1

Buck, K.N., Sedwick, P.N., Sohst, B., Carlson, C.A., 2018. Organic complexation of iron in the eastern tropical South Pacific: Results from US GEOTRACES Eastern Pacific Zonal Transect (GEOTRACES cruise GP16). Mar. Chem. 201, 229–241. doi:10.1016/j.marchem.2017.11.007

Burton, J.D., Culkin, F., 1972. Gallium, in: Wedepohl, K.H. (Ed.), Handbook of Geochemistry. Spring-Verlag, p. Parts B-O.

Chaigneau, A., Dominguez, N., Eldin, G., Vasquez, L., Flores, R., Grados, C., Echevin, V., 2013. Near-coastal circulation in the Northern Humboldt Current System from shipboard ADCP data. J. Geophys. Res. Ocean. 118, 5251–5266. doi:10.1002/jgrc.20328

Collier, R., Edmond, J., 1984. The trace element geochemistry of marine biogenic particulate matter. Prog. Oceanogr. 13, 113–199. doi:10.1016/0079-6611(84)90008-9

Cutter, G.A., Bruland, K.W., 2012. Rapid and noncontaminating sampling system for trace elements in global ocean surveys. Limnol. Oceanogr. Methods 10, 425–436. doi:10.4319/lom.2012.10.425

Cutter, G., Andersson, P., Codispoti, L., Croot, P., Francois, R., Lohan, M., Obata, H., Rutgers v. d. Loeff, M., 2014. Sampling and sample-handling protocols for GEOTRACES Cruises, v2.0.

Dammshäuser, A., Wagener, T., Garbe-Schönberg, D., Croot, P., 2013. Particulate and dissolved aluminum and titanium in the upper water column of the Atlantic Ocean. Deep. Res. Part I Oceanogr. Res. Pap. 73, 127–139. doi:10.1016/j.dsr.2012.12.002

Donaghay, P.L., Liss, P.S., Duce, R.A., Kester, D.R., Hanson, A.K., Villareal, T., Tindale, N.W., Gifford, D.J., 1991. The role of episodic atmospheric nutrient inputs in the chemical and biological dynamics od oceanic ecosystems. Oceanography 4, 62-70. doi.org/10.5670/oceanog.1991.04.

1005 Elderfield, H., Schultz, A., 1996. Mid-Ocean Ridge hydrothermal fluxes and the chemical composition of the Ocean.
1006 Annu. Rev. Earth Planet. Sci. 24, 191–224. doi:10.1146/annurev.earth.24.1.191

1007 Emery, T., 1986. Exchange of iron by gallium in siderophores. Biochemistry 25, 4629–4633.
1008 doi:10.1021/bi00364a026

1009 Emery, T., Hoffer, P.B., 1980. Siderophore-mediated mechanism of gallium uptake demonstrated in the
1010 microorganism Ustilago sphaerogena. J. Nucl. Med. 21, 935–939.

1011 Fitzsimmons, J.N., John, S.G., Marsay, C.M., Hoffman, C.L., Nicholas, S.L., Toner, B.M., German, C.R., Sherrell,
1012 R.M., 2017. Iron persistence in a distal hydrothermal plume supported by dissolved-particulate exchange. Nat.
1013 Geosci 10, 195–201. doi:10.1038/ngeo2900

1014 Gaillardet, J., Viers, J., Dupré, B., 2014. 7.7 - Trace Elements in River Waters, in: Holland, H.D., Turekian, K.K.
1015 (Eds.), Treatise on Geochemistry (Second Edition). Elsevier, Oxford, pp. 195–235. doi:10.1016/B978-0-08-
1016 095975-7.00507-6

1017 Gamo, T., Sakai, H., Ishibashi, J., Nakayama, E., Isshiki, K., Matsuura, H., Shitashima, K., Takeuchi, K., Ohta, S.,
1018 1993. Hydrothermal plumes in the eastern Manus Basin, Bismarck Sea: CH4, Mn, Al and pH anomalies. Deep
1019 Sea Res. Part I Oceanogr. Res. Pap. 40, 2335–2349. doi:10.1016/0967-0637(93)90108-F

1020 Gascoyne, D.J., Connor, J.A., Bull, A.T., 1991. Isolation of bacteria producing siderophores under alkaline
1021 conditions. Appl. Microbiol. Biotechnol. 36, 130–135. doi:10.1007/BF00164713

1022 Gehlen, M., Beck, L., Calas, G., Flank, A.M., Van Bennekom, A.J., Van Beusekom, J.E.E., 2002. Unraveling the
1023 atomic structure of biogenic silica: Evidence of the structural association of Al and Si in diatom frustules.
1024 Geochim. Cosmochim. Acta 66, 1601–1609. doi:10.1016/S0016-7037(01)00877-8

1025 German, C.R., Seyfried Jr., W.E., 2014. 8.7 - Hydrothermal Processes, in: Holland, H.D., Turekian, K.L. (Eds.),
1026 Treatise on Geochemistry (Second Edition). Elsevier, Oxford, pp. 191–233. doi:10.1016/B978-0-08-095975-
1027 7.00607-0

1028 Grand, M.M., Buck, C.S., Landing, W.M., Measures, C.I., Hatta, M., Hiscock, W.T., Brown, M., Resing, J.A., 2014.
1029 Quantifying the Impact of Atmospheric Deposition on the Biogeochemistry of Fe and Al in the. Oceanography
1030 27, 62–65.

1031 Grand, M.M., Measures, C.I., Hatta, M., Hiscock, W.T., Landing, W.M., Morton, P.L., Buck, C.S., Barrett, P.M.,
1032 Resing, J.A., 2015. Dissolved Fe and Al in the upper 1000m of the eastern Indian Ocean: A high-resolution
1033 transect along 95°E from the Antarctic margin to the Bay of Bengal. Global Biogeochem. Cycles 1–22.
1034 doi:10.1002/2014GB004920.

1035 Han, Q., Moore, J.K., Zender, C., Measures, C., Hydes, D., 2008. Constraining oceanic dust deposition using surface
1036 ocean dissolved Al. Global Biogeochem. Cycles 22. doi:10.1029/2007gb002975

1037 Hatta, M., Measures, C.I., Selph, K.E., Zhou, M., Hiscock, W.T., 2013. Iron fluxes from the shelf regions near the
1038 South Shetland Islands in the Drake Passage during the austral-winter 2006. Deep. Res. Part II Top. Stud.
1039 Oceanogr. 90, 89–101. doi:10.1016/j.dsr2.2012.11.003

1040 Hatta, M., Measures, C.I., Wu, J., Roshan, S., Fitzsimmons, J.N., Sedwick, P., Morton, P., 2015. An overview of
1041 dissolved Fe and Mn distributions during the 2010–2011 U.S. GEOTRACES north Atlantic cruises:
1042 GEOTRACES GA03. Deep Sea Res. Part II Top. Stud. Oceanogr. 116, 117–129.
1043 doi:10.1016/j.dsr2.2014.07.005

1044 Hawco, N.J., Ohnemus, D.C., Resing, J.A., Twining, B.S., Saito, M.A., 2016. A dissolved cobalt plume in the
1045 oxygen minimum zone of the eastern tropical South Pacific. Biogeosciences 13, 5697–5717. doi:10.5194/bg-

1046 Hayes, C.T., Anderson, R.F., Fleisher, M.Q., Huang, K.F., Robinson, L.F., Lu, Y., Cheng, H., Edwards, R.L.,
1047 Moran, S.B., 2015. ^{230}Th and ^{231}Pa on GEOTRACES GA03, the U.S. GEOTRACES North Atlantic transect,
1048 and implications for modern and paleoceanographic chemical fluxes. Deep. Res. Part II Top. Stud. Oceanogr.

116, 29–41. doi:10.1016/j.dsr2.2014.07.007

Hydes, D.J., Liss, P.S., 1977. The behaviour of dissolved aluminium in estuarine and coastal waters. Estuar. Coast. Mar. Sci. 5, 755–769. doi:10.1016/0302-3524(77)90047-0

Hydes, D.J., 1979. Aluminum in seawater : Control by inorganic processes. Science 205, 1260–1262.

Hydes, D.J., 1983. Distribution of aluminium in waters of the North East Atlantic 25°N to 35°N. Geochim. Cosmochim. Acta 47, 967–973. doi:10.1016/0016-7037(83)90164-3

Hydes, D.J., 1989. Seasonal variation in dissolved aluminium concentrations in coastal waters and biological limitation of the export of the riverine input of aluminium to the deep sea. Cont. Shelf Res. 9, 919–929. doi:10.1016/0278-4343(89)90065-4

Jenkins, W.J., Lott, D.E., Longworth, B.E., Curtice, J.M., Cahill, K.L., 2015. The distributions of helium isotopes and tritium along the U.S. GEOTRACES North Atlantic sections (GEOTRACES GAO3). Deep. Res. Part II Top. Stud. Oceanogr. 116, 21–28. doi:10.1016/j.dsr2.2014.11.017

Jenkins, W.J., Lott, D.E., German, C.R., Cahill, K.L., Goudreau, J., Longworth, B., 2018. The deep distributions of helium isotopes, radiocarbon, and noble gases along the U.S. GEOTRACES East Pacific Zonal Transect (GP16). Mar. Chem. 201, 167–182. doi:10.1016/j.marchem.2017.03.009

Jickells, T., Church, T., Veron, A., Arimoto, R., 1994. Atmospheric inputs of manganese and aluminium to the Sargasso Sea and their relation to surface water concentrations. Mar. Chem. 46, 283–292. doi:10.1016/0304-4203(94)90083-3

Jickells, T.D., An, Z.S., Andersen, K.K., Baker, A.R., Bergametti, G., Brooks, N., Cao, J.J., Boyd, P.W., Duce, R.A., Hunter, K.A., Kawahata, H., Kubilay, N., laRoche, J., Liss, P.S., Mahowald, N., Prospero, J.M., Ridgwell, A.J., Tegen, I., Torres, R., 2005. Global Iron Connections Between Desert Dust, Ocean Biogeochemistry, and Climate. Science 308, 67–71. doi:10.1126/science.1105959

John, S.G., Helgoe, J., Townsend, E., Weber, T., DeVries, T., Tagliabue, A., Moore, K., Lam, P., Marsay, C.M., Till, C., 2018. Biogeochemical cycling of Fe and Fe stable isotopes in the Eastern Tropical South Pacific. Mar. Chem. 201, 66–76. doi:10.1016/j.marchem.2017.06.003

Johnson, K.S., Elrod, V.A., Fitzwater, S.E., Plant, J.N., Chavez, F.P., Tanner, S.J., Gordon, R.M., Westphal, D.L., Perry, K.D., Wu, J., Karl, D.M., 2003. Surface ocean-lower atmosphere interactions in the Northeast Pacific Ocean Gyre: Aerosols, iron, and the ecosystem response. Global Biogeochem. Cycles 17, 1063. doi:10.1029/2002GB002004

Koning, E., Gehlen, M., Flank, A.M., Calas, G., Epping, E., 2007. Rapid post-mortem incorporation of aluminum in diatom frustules: Evidence from chemical and structural analyses. Mar. Chem. 103, 97–111. doi:10.1016/j.marchem.2006.09.001

Kramer, J., Laan, P., Sarthou, G., Timmermans, K.R., De Baar, H.J.W., 2004. Distribution of dissolved aluminium in the high atmospheric input region of the subtropical waters of the North Atlantic Ocean. Mar. Chem. 88, 85–101. doi:10.1016/j.marchem.2004.03.009

Kremling, K., 1985. The distribution of cadmium, copper, nickel, manganese, and aluminium in surface waters of the open Atlantic and European shelf area. Deep Sea Res. Part A. Oceanogr. Res. Pap. 32, 531–555. doi:10.1016/0198-0149(85)90043-3

Lam, P.J., Lee, J.M., Heller, M.I., Mehic, S., Xiang, Y., Bates, N.R., 2018. Size-fractionated distributions of suspended particle concentration and major phase composition from the U.S. GEOTRACES Eastern Pacific Zonal Transect (GP16). Mar. Chem. 201, 90–107. doi:10.1016/j.marchem.2017.08.013

Lee, J.M., Heller, M.I., Lam, P.J., 2018. Size distribution of particulate trace elements in the U.S. GEOTRACES Eastern Pacific Zonal Transect (GP16). Mar. Chem. 201, 108–123. doi:10.1016/j.marchem.2017.09.006

1092 Li, F.M., Ren, J.L., Yan, L., Liu, S.M., Liu, C.G., Zhou, F., Zhang, J., 2013. The biogeochemical behavior of
1093 dissolved aluminum in the southern Yellow Sea: Influence of the spring phytoplankton bloom. Chinese Sci.
1094 Bull. 58, 238–248. doi:10.1007/s11434-012-5512-5

1095 Lonsdale, P., 1976. Abyssal circulation of the southeastern Pacific and some geological implications. J. Geophys.
1096 Res. 81, 1163–1176. doi:10.1029/JC081i006p01163

1097 Lunel, T., Rudnicki, M., Elderfield, H., Hydes, D., 1990. Aluminium as a depth-sensitive tracer of entrainment in
1098 submarine hydrothermal plumes. Nature 344, 137–139. doi:10.1038/344137a0

1099 Lupton, J.E.J., Baker, E.T.E., Mottl, M.J., Sansone, F.J., Wheat, C.G., Resing, J.A., Massoth, G.J., Measures, C.I.,
1100 Feely, R.A., 1993. Chemical and physical diversity of hydrothermal plumes along the East Pacific Rise, Rise,
1101 8° 45′ N to 11° 50′ N. Geophys. Res. Lett. 20, 2913-2916. doi: 10.1029/93GL00906.

1102 Mahowald, N.M., Baker, A.R., Bergametti, G., Brooks, N., Duce, R.A., Jickells, T.D., Kubilay, N., Prospero, J.M.,
1103 Tegen, I., 2005. Atmospheric global dust cycle and iron inputs to the ocean. Global Biogeochem. Cycles 19,
1104 GB4025. doi:10.1029/2004gb002402

1105 Marchig, V., Von Stackelberg, U., Wiedicke, M., Durn, G., Milovanovic, D., 1999. Hydrothermal activity
1106 associated with off-axis volcanism in the Peru Basin. Mar. Geol. 159, 179–203. doi:10.1016/S0025-
1107 3227(98)00193-5

1108 McAlister, J., Orians, K., 2012. Calculation of river-seawater endmembers and differential trace metal scavenging in
1109 the Columbia River plume. Estuar. Coast. Shelf Sci. 99, 31–41. doi:10.1016/j.ecss.2011.12.013

1110 McMurtry, G.M., Burnett, W.C., 1975. Hydrothermal metallogenesis in the Bauer Deep of the south-eastern Pacific.
1111 Nature 254, 42–44.

1112 Measures, C.I., Grant, B., Khadem, M., Lee, D.S., Edmond, J.M., 1984. Distribution of Be, Al, Se and Bi in the
1113 surface waters of the western North Atlantic and Caribbean. Earth Planet. Sci. Lett. 71, 1–12.
1114 doi:10.1016/0012-821X(84)90047-5

1115 Measures, C.I., Edmond, J.M., Jickells, T.D., 1986. Aluminium in the northwest Atlantic. Geochim. Cosmochim.
1116 Acta 50, 1423–1429. doi:10.1016/0016-7037(86)90315-7

1117 Measures, C.I., Edmond, J.M., 1990. Aluminium in the South Atlantic: Steady state distribution of a short residence
1118 time element. J. Geophys. Res. Ocean. 95, 5331–5340. doi:10.1029/JC095iC04p05331

1119 Measures, C.I., 1995. The distribution of Al in the IOC stations of the eastern Atlantic between 30° S and 34° N.
1120 Mar. Chem. 49, 267–281. doi:10.1016/0304-4203(95)00017-L

1121 Measures, C.I., Brown, E.T., 1996. Estimating dust input to the Atlantic Ocean using surface water aluminium
1122 concentrations, in: Guerzoni, S., Chester, R. (Eds.), The Impact of Desert Dust Across the Mediterranean.
1123 Springer Netherlands, Dordrecht, pp. 301–311. doi:10.1007/978-94-017-3354-0_30

1124 Measures, C.I., Brown, M.T., Vink, S., 2005. Dust deposition to the surface waters of the western and central North
1125 Pacific inferred from surface water dissolved aluminum concentrations. Geochemistry, Geophys. Geosystems
1126 6, Q09M03. doi:10.1029/2005gc000922

1127 Measures, C.I., Landing, W.M., Brown, M.T., Buck, C.S., 2008a. High-resolution Al and Fe data from the Atlantic
1128 Ocean CLIVAR-CO_2 repeat hydrography A16N transect: Extensive linkages between atmospheric dust and
1129 upper ocean geochemistry. Global Biogeochem. Cycles 22, GB1005. doi:10.1029/2007gb003042

1130 Measures, C.I., Landing, W.M., Brown, M.T., Buck, C.S., 2008b. A commercially available rosette system for trace
1131 metal-clean sampling. Limnol. Oceanogr. Methods 6, 384–394.

1132 Measures, C.I., Sato, T., Vink, S., Howell, S., Li, Y.H., 2010. The fractional solubility of aluminium from mineral
1133 aerosols collected in Hawaii and implications for atmospheric deposition of biogeochemically important trace
1134 elements. Mar. Chem. 120, 144–153. doi:10.1016/j.marchem.2009.01.014

1135 Measures, C., Hatta, M., Fitzsimmons, J., Morton, P., 2015. Dissolved Al in the zonal N Atlantic section of the US
1136 GEOTRACES 2010/2011 cruises and the importance of hydrothermal inputs. Deep Sea Res. Part II Top. Stud.
1137 Oceanogr. 116, 176–186. doi:10.1016/j.dsr2.2014.07.006

1138 Metz, S., Trefry, J.H., 2000. Chemical and mineralogical influences on concentrations of trace metals in
1139 hydrothermal fluids. Geochim. Cosmochim. Acta 64, 2267–2279. doi:10.1016/S0016-7037(00)00354-9

1140 Middag, R., de Baar, H.J.W., Laan, P., Bakker, K., 2009. Dissolved aluminium and the silicon cycle in the Arctic
1141 Ocean. Mar. Chem. 115, 176–195. doi:10.1016/j.marchem.2009.08.002

1142 Middag, R., van Slooten, C., de Baar, H.J.W., Laan, P., 2011. Dissolved aluminium in the Southern Ocean. Deep
1143 Sea Res. Part II Top. Stud. Oceanogr. 58, 2647–2660. doi:10.1016/j.dsr2.2011.03.001

1144 Middag, R., De Baar, H.J.W., Laan, P., Huhn, O., 2012. The effects of continental margins and water mass
1145 circulation on the distribution of dissolved aluminum and manganese in Drake Passage. J. Geophys. Res.
1146 Ocean. 117, 1–19. doi:10.1029/2011JC007434

1147 Middag, R., de Baar, H.J.W., Klunder, M.B., Laan, P., 2013. Fluxes of dissolved aluminum and manganese to the
1148 Weddell Sea and indications for manganese co-limitation. Limnol. Oceanogr. 58, 287–300.
1149 doi:10.4319/lo.2013.58.1.0287

1150 Middag, R., van Hulten, M.M.P., Van Aken, H.M., Rijkenberg, M.J.A., Gerringa, L.J.A., Laan, P., de Baar, H.J.W.,
1151 2015. Dissolved aluminium in the ocean conveyor of the West Atlantic Ocean: Effects of the biological cycle,
1152 scavenging, sediment resuspension and hydrography. Mar. Chem. 177, 69–86.
1153 doi:10.1016/j.marchem.2015.02.015

1154 Moran, S.B., Moore, R.M., 1988. Temporal variations in dissolved and particulate aluminum during a spring bloom.
1155 Estuar. Coast. Shelf Sci. 27, 205–215. doi:10.1016/0272-7714(88)90090-X

1156 Moran, S.B., Moore, R.M., 1991. The potential source of dissolved aluminum from resuspended sediments to the
1157 North Atlantic Deep Water. Geochim. Cosmochim. Acta 55, 2745–2751. doi:10.1016/0016-7037(91)90441-7

1158 Moran, S.B., Moore, R.M., 1992. Kinetics of the removal of dissolved aluminum by diatoms in seawater: A
1159 comparison with thorium. Geochim. Cosmochim. Acta 56, 3365–3374. doi:10.1016/0016-7037(92)90384-U

1160 Morris, A.W., Howland, R.J.M., Bale, A.J., 1986. Dissolved aluminium in the Tamar Estuary, southwest England.
1161 Geochim. Cosmochim. Acta 50, 189–197. doi:10.1016/0016-7037(86)90168-7

1162 Mottl, M.J., 2003. Partitioning of Energy and Mass Fluxes between Mid-ocean Ridge Axes and Flanks at High and
1163 Low Temperature, in: Halbach, P.E., Tunnicliffe, V., Hein, J.R. (Eds.), Energy and Mass Transfer in Marine
1164 Hydrothermal Systems. Dahlem University Press, Berline, pp. 271–286.

1165 Obata, H., Nozaki, Y., Alibo, D.S., Yamamoto, Y., 2004. Dissolved Al, In, and Ce in the eastern Indian Ocean and
1166 the Southeast Asian Seas in comparison with the radionuclides210Pb and210Po. Geochim. Cosmochim. Acta
1167 68, 1035–1048. doi:10.1016/j.gca.2003.07.021

1168 Ohnemus, D.C., Lam, P.J., 2015. Cycling of lithogenic marine particles in the US GEOTRACES North Atlantic
1169 transect. Deep Sea Res. Part II Top. Stud. Oceanogr. 116, 283–302. doi:10.1016/j.dsr2.2014.11.019

1170 Ohnemus, D.C., Rauschenberg, S., Cutter, G.A., Fitzsimmons, J.N., Sherrell, R.M., Twining, B.S., 2017. Elevated
1171 trace metal content of prokaryotic communities associated with marine oxygen deficient zones. Limnol.
1172 Oceanogr. 62, 3–25. doi:10.1002/lno.10363

1173 Ohnemus, D.C., Lam, P.J., Twining, B.S., 2018. Optical observation of particles and responses to particle
1174 composition in the GEOTRACES GP16 section. Mar. Chem. 201, 124–136.
1175 doi:10.1016/j.marchem.2017.09.004

1176 Orians, K.J., Bruland, K.W., 1985. Dissolved aluminium in the central North Pacific. Nature 316, 427.

1177 Orians, K.J., Bruland, K.W., 1986. The biogeochemistry of aluminum in the Pacific Ocean. Earth Planet. Sci. Lett.
1178 78, 397–410. doi:10.1016/0012-821X(86)90006-3

1179 Orians, K.J., Bruland, K.W., 1988a. The marine geochemistry of dissolved gallium: A comparison with dissolved
1180 aluminum. Geochim. Cosmochim. Acta 52, 2955–2962.

1181 Orians, K.J., Bruland, K.W., 1988b. Dissolved gallium in the open ocean. Nature 332, 717–719.

1182 Pavia, F., Anderson, R., Vivancos, S., Fleisher, M., Lam, P., Lu, Y., Cheng, H., Zhang, P., Lawrence Edwards, R.,
1183 2018. Intense hydrothermal scavenging of ^{230}Th and ^{231}Pa in the deep Southeast Pacific. Mar. Chem. 201,
1184 212–228. doi:10.1016/j.marchem.2017.08.003

1185 Perdue, E.M., Beck, K.C., Helmut Reuter, J., 1976. Organic complexes of iron and aluminium in natural waters.
1186 Nature 260, 418.

1187 Peters, B.D., Jenkins, W.J., Swift, J.H., German, C.R., Moffett, J.W., Cutter, G.A., Brzezinski, M.A., Casciotti,
1188 K.L., 2018. Water mass analysis of the 2013 US GEOTRACES eastern Pacific zonal transect (GP16). Mar.
1189 Chem. 201, 6–19. doi:10.1016/j.marchem.2017.09.007

1190 Reid, J.L., 1997. On the total geostrophic circulation of the pacific ocean: flow patterns, tracers, and transports.
1191 Prog. Oceanogr. 39, 263–352. doi:10.1016/S0079-6611(97)00012-8

1192 Resing, J.A., Measures, C.I., 1994. Fluorometric determination of Al in seawater by flow injection analysis with in-
1193 line preconcentration. Anal. Chem. 66, 4105–4111. doi:10.1021/ac00094a039

1194 Resing, J.A., Sedwick, P.N., German, C.R., Jenkins, W.J., Moffett, J.W., Sohst, B.M., Tagliabue, A., 2015. Basin-
1195 scale transport of hydrothermal dissolved metals across the South Pacific Ocean. Nature 523, 200–203.
1196 doi:10.1038/nature14577

1197 Revels, B.N., Ohnemus, D.C., Lam, P.J., Conway, T.M., John, S.G., 2015. The isotopic signature and distribution of
1198 particulate iron in the North Atlantic Ocean. Deep. Res. Part II Top. Stud. Oceanogr. 116, 321–331.
1199 doi:10.1016/j.dsr2.2014.12.004

1200 Rudnick, R.L., Gao, S., 2014. 4.1 - Composition of the Continental Crust, in: Holland, H.D., Turekian, K.K. (Eds.),
1201 Treatise on Geochemistry (Second Edition). Elsevier, Oxford, pp. 1–51. doi:10.1016/B978-0-08-095975-
1202 7.00301-6

1203 Sanial, V., Kipp, L.E., Henderson, P.B., van Beek, P., Reyss, J.L., Hammond, D.E., Hawco, N.J., Saito, M.A.,
1204 Resing, J.A., Sedwick, P., Moore, W.S., Charette, M.A., 2018. Radium-228 as a tracer of dissolved trace
1205 element inputs from the Peruvian continental margin. Mar. Chem. 201, 20–34.
1206 doi:10.1016/j.marchem.2017.05.008

1207 Schlitzer, R., 2016. Quantifying He fluxes from the mantle using multi-tracer data assimilation. Philos. Trans. R.
1208 Soc. A Math. Phys. Eng. Sci. 374, 20150288. doi:10.1098/rsta.2015.0288

1209 Schlitzer, R., Anderson, R.F., Dodas, E.M., Lohan, M., Geibert, W., Tagliabue, A., Bowie, A., Jeandel, C.,
1210 Maldonado, M.T., Landing, W.M., Cockwell, D., Abadie, C., Abouchami, W., Achterberg, E.P., Agather, A.,
1211 Aguliar-Islas, A., van Aken, H.M., Andersen, M., Archer, C., Auro, M., de Baar, H.J., Baars, O., Baker, A.R.,
1212 Bakker, K., Basak, C., Baskaran, M., Bates, N.R., Bauch, D., van Beek, P., Behrens, M.K., Black, E., Bluhm,
1213 K., Bopp, L., Bouman, H., Bowman, K., Bown, J., Boyd, P., Boye, M., Boyle, E.A., Branellec, P., Bridgestock,
1214 L., Brissebrat, G., Browning, T., Bruland, K.W., Brumsack, H.-J., Brzezinski, M., Buck, C.S., Buck, K.N.,
1215 Buesseler, K., Bull, A., Butler, E., Cai, P., Mor, P.C., Cardinal, D., Carlson, C., Carrasco, G., Casacuberta, N.,
1216 Casciotti, K.L., Castrillejo, M., Chamizo, E., Chance, R., Charette, M.A., Chaves, J.E., Cheng, H., Chever, F.,
1217 Christl, M., Church, T.M., Closset, I., Colman, A., Conway, T.M., Cossa, D., Croot, P., Cullen, J.T., Cutter,
1218 G.A., Daniels, C., Dehairs, F., Deng, F., Dieu, H.T., Duggan, B., Dulaquais, G., Dumousseaud, C., Echegoyen-
1219 Sanz, Y., Edwards, R.L., Ellwood, M., Fahrbach, E., Fitzsimmons, J.N., Russell Flegal, A., Fleisher, M.Q., van
1220 de Flierdt, T., Frank, M., Friedrich, J., Fripiat, F., Fröllje, H., Galer, S.J.G., Gamo, T., Ganeshram, R.S.,

Garcia-Orellana, J., Garcia-Solsona, E., Gault-Ringold, M., George, E., Gerringa, L.J.A., Gilbert, M., Godoy, J.M., Goldstein, S.L., Gonzalez, S.R., Grissom, K., Hammerschmidt, C., Hartman, A., Hassler, C.S., Hathorne, E.C., Hatta, M., Hawco, N., Hayes, C.T., Heimbürger, L.-E., Helgoe, J., Heller, M., Henderson, G.M., Henderson, P.B., van Heuven, S., Ho, P., Horner, T.J., Hsieh, Y.-T., Huang, K.-F., Humphreys, M.P., Isshiki, K., Jacquot, J.E., Janssen, D.J., Jenkins, W.J., John, S., Jones, E.M., Jones, J.L., Kadko, D.C., Kayser, R., Kenna, T.C., Khondoker, R., Kim, T., Kipp, L., Klar, J.K., Klunder, M., Kretschmer, S., Kumamoto, Y., Laan, P., Labatut, M., Lacan, F., Lam, P.J., Lambelet, M., Lamborg, C.H., Le Moigne, F.A.C., Le Roy, E., Lechtenfeld, O.J., Lee, J.-M., Lherminier, P., Little, S., López-Lora, M., Lu, Y., Masque, P., Mawji, E., Mcclain, C.R., Measures, C., Mehic, S., Barraqueta, J.-L.M., van der Merwe, P., Middag, R., Mieruch, S., Milne, A., Minami, T., Moffett, J.W., Moncoiffe, G., Moore, W.S., Morris, P.J., Morton, P.L., Nakaguchi, Y., Nakayama, N., Niedermiller, J., Nishioka, J., Nishiuchi, A., Noble, A., Obata, H., Ober, S., Ohnemus, D.C., van Ooijen, J., O'Sullivan, J., Owens, S., Pahnke, K., Paul, M., Pavia, F., Pena, L.D., Peters, B., Planchon, F., Planquette, H., Pradoux, C., Puigcorbé, V., Quay, P., Queroue, F., Radic, A., Rauschenberg, S., Rehkämper, M., Rember, R., Remenyi, T., Resing, J.A., Rickli, J., Rigaud, S., Rijkenberg, M.J.A., Rintoul, S., Robinson, L.F., Roca-Martí, M., Rodellas, V., Roeske, T., Rolison, J.M., Rosenberg, M., Roshan, S., Rutgers van der Loeff, M.M., Ryabenko, E., Saito, M.A., Salt, L.A., Sanial, V., Sarthou, G., Schallenberg, C., Schauer, U., Scher, H., Schlosser, C., Schnetger, B., Scott, P., Sedwick, P.N., Semiletov, I., Shelley, R., Sherrell, R.M., Shiller, A.M., Sigman, D.M., Singh, S.K., Slagter, H.A., Slater, E., Smethie, W.M., Snaith, H., Sohrin, Y., Sohst, B., Sonke, J.E., Speich, S., Steinfeldt, R., Stewart, G., Stichel, T., Stirling, C.H., Stutsman, J., Swarr, G.J., Swift, J.H., Thomas, A., Thorne, K., Till, C.P., Till, R., Townsend, A.T., Townsend, E., Tuerena, R., Twining, B.S., Vance, D., Velazquez, S., Venchiarutti, C., Villa-Alfageme, M., Vivancos, S.M., Voelker, A.H.L., Wake, B., Warner, M.J., Watson, R., van Weerlee, E., Alexandra Weigand, M., Weinstein, Y., Weiss, D., Wisotzki, A., Woodward, E.M.S., Wu, J., Wu, Y., Wuttig, K., Wyatt, N., Xiang, Y., Xie, R.C., Xue, Z., Yoshikawa, H., Zhang, J., Zhang, P., Zhao, Y., Zheng, L., Zheng, X.-Y., Zieringer, M., Zimmer, L.A., Ziveri, P., Zunino, P., Zurbrick, C., 2018. The GEOTRACES Intermediate Data Product 2017. Chem. Geol. doi: 10.1016/j.chemgeo.2018.05.040

Shelley, R.U., Landing, W.M., Ussher, S.J., Planquette, H., Sarthou, G., 2018. Regional trends in the fractional solubility of Fe and other metals from North Atlantic aerosols (GEOTRACES cruises GA01 and GA03) following a two-stage leach. Biogeosciences 155194, 2271–2288. doi:10.5194/bg-15-2271-2018

Shiller, A.M., 1988. Enrichment of dissolved gallium relative to aluminum in natural waters. Geochim. Cosmochim. Acta 52, 1879–1882. doi:10.1016/0016-7037(88)90011-7

Shiller, A.M., Frilot, D.M., 1996. The geochemistry of gallium relative to aluminum in Californian streams. Geochim. Cosmochim. Acta 60, 1323–1328. doi:10.1016/0016-7037(96)00002-6

Shiller, A.M., 1998. Dissolved gallium in the Atlantic Ocean. Mar. Chem. 61, 87–99. doi:10.1016/s0304-4203(98)00009-7

Shiller, A.M., Bairamadgi, G.R., 2006. Dissolved gallium in the northwest Pacific and the south and central Atlantic Oceans: Implications for aeolian Fe input and a reconsideration of profiles. Geochemistry Geophys. Geosystems 7. doi:10.1029/2005gc001118

Shiller, A.M., Hatta, M., Measures, C.I., 2014. Dissolved gallium and gallium/aluminum ratios in the US GEOTRACES North Atlantic zonal section. Presented at Ocean Scieces Meeting, Honolulu, HI, March 2014. (oral) Abstract ID: 15331; http://www.sgmeet.com/osm2014/viewabstract.asp?AbstractID=15331.

Sholkovitz, E.R., 1978. The flocculation of dissloved Fe, Mn, Al, Cu, Ni, Co and Cd during estuarine mixing. Earth Planet. Sci. Lett. 41, 77–86.

Stoffyn, M., Mackenzie, F.T., 1982. Fate of dissolved aluminum in the oceans. Mar. Chem. 11, 105–127. doi:10.1016/0304-4203(82)90036-6

Strub, P.T., Mesias, J.M., Montecino, V., Rutllant, J., Salinas, S., 1998. Coastal ocean circulation off western South America, in: Robinson, A.R., Brink, K.H. (Eds.), The Sea. John Wiley, Hoboken, N. J., pp. 273–314.

1268 Stumm, W., Morgan, J., 1996. Aquatic Chemistry: Chemical Equilibria and Rates in Natural Waters. John Wiley &
1269 Sons, New York.

1270 Takayanagi, K., Gobeil, C., 2000. Dissolved aluminum in the upper St. Lawrence estuary. J. Oceanogr. 56, 517–525.
1271 doi:10.1023/A:1011196826709

1272 Talley, L.D., Pickard, G.L., Emery, W.J., Swift, J.H., 2011. Descriptive Physical Oceanography: An Introduction,
1273 Sixth. ed. Elsevier, Boston.

1274 Tipping, E., Rey-Castro, C., Bryan, S.E., Hamilton-Taylor, J., 2002. Al(III) and Fe(III) binding by humic substances
1275 in freshwaters, and implications for trace metal speciation. Geochim. Cosmochim. Acta 66, 3211–3224.

1276 Van Bennekom, A.J., Jager, J.E., 1978. Dissolved aluminium in the Zaire river plume. Netherlands J. Sea Res. 12,
1277 358–367. doi:10.1016/0077-7579(78)90039-X

1278 Van Beusekom, J.E.E., Van Bennekom, A.J., Tréguer, P., Morvan, J., 1997. Aluminium and silicic acid in water and
1279 sediments of the Enderby and Crozet Basins. Deep. Res. Part II Top. Stud. Oceanogr. 44, 987–1003.
1280 doi:10.1016/S0967-0645(96)00105-1

1281 Von Damm, K., Edmond, J.M., Measures, C.I., Grant, B., 1985. Chemistry of submarine hydrothermal solutions at
1282 Guaymas Basin, Gulf of California. Geochim. Cosmochim. Acta 49, 2221–2237.

1283 Wu, J.F., Boyle, E.A., 1997. Low blank preconcentration technique for the determination of lead, copper, and
1284 cadmium in small-volume seawater samples by isotope dilution ICPMS. Anal. Chem. 69, 2464–2470.
1285 doi:10.1021/ac961204u

1286 Wu, J., Boyle, E.A., 1998. Determination of iron in seawater by high-resolution isotope dilution inductively coupled
1287 plasma mass spectrometry after $Mg(OH)_2$ coprecipitation. Anal. Chim. Acta 367, 183–191.
1288 doi:10.1016/S0003-2670(98)00145-7

1289 Wuttig, K., Wagener, T., Bressac, M., Dammshäuser, A., Streu, P., Guieu, C., Croot, P.L., 2013. Impacts of dust
1290 deposition on dissolved trace metal concentrations (Mn, Al and Fe) during a mesocosm experiment.
1291 Biogeosciences 10, 2583–2600. doi:10.5194/bg-10-2583-2013

1292 Wyrtki, K., 1966. Ocaenography of the eastern equatorial Pacific Ocean. Ocean. Mar. Biol. Ann. Rev. 4, 33–68.

1293 Zhang, Y., Mahowald, N., Scanza, R.A., Journet, E., Desboeufs, K., Albani, S., Kok, J.F., Zhuang, G., Chen, Y.,
1294 Cohen, D.D., Paytan, A., Patey, M.D., Achterberg, E.P., Engelbrecht, J.P., Fomba, K.W., 2015. Modeling the
1295 global emission, transport and deposition of trace elements associated with mineral dust. Biogeosciences 12,
1296 5771–5792. doi:10.5194/bg-12-5771-2015

1297